Behaviour of dissimilar welded T-joints made of duplex and carbon steel under atmospheric corrosion

Shuang Sun

St Anne's College, University of Oxford

A thesis submitted for the degree of

MSc by Research

Trinity 2023

ABSTRACT

This paper investigates the corrosion behaviour of dissimilar welds between duplex stainless steel and carbon steel under atmospheric environments. Duplex stainless steel grade EN1.4062 was welded to two different carbon steel grades S355J2 and P460NL2 by means of gas metal arc welding (GMAW) to form T-joints. The fabricated specimens were subjected to 12-month exposure tests in 4 different atmospheric environments, distributed across 3 different countries: Belgium, England, and Portugal. A total of 84 samples were designed, fabricated and sand blasted, in order to satisfy the surface requirements of ISO 8501-1 [1]. Exposure racks were assembled to expose a range of samples to the weather conditions at each test location following the same methodology. The environmental parameters influencing the corrosion behaviour of dissimilar welds were monitored on a continuous basis and correlated to the respective corrosion rates. Uniform, pitting, and galvanic corrosion were studied. Based on these measurements, guidance was given on the necessary protective coating for such welds in the context of applications in structures.

*This thesis is dedicated to my partner **Yu WENG**,*

*to my parents, **Ruihua SUN** and **Yuxia LI**, and to my family in China.*

Their endless love and support are what made me the person that I am today. I would not be standing at the end of this long journey if it were not for them.

ACKNOWLEDGEMENTS

I would like to express my deepest gratitude to the following people:

First and foremost, I am profoundly thankful to my supervisor, **Barbara Rossi**, for her unwavering encouragement, remarkable patience, and invaluable guidance throughout my research studies. I am grateful for the productive and enlightening conversations we had during our regular Friday meetings.

To **Burak Karabulut**, who was always there during my research journey. Your insightful advice and expertise have played a pivotal role in driving this work forward. Thank you for the sandwiches during those laboratory afternoons at KU Leuven. To **Brent Verhoeven**, for his guidance and assistance during my experimental operations. Your willingness to engage in meaningful discussions has been invaluable to me. To **Gonçalo Ferraz**, for the rich inspiration and advice he has provided in the beginning of my work. Your extensive knowledge and experience in welding have been instrumental in shaping this work.

I would especially like to thank **Raf Dewil**, for providing the experimental site in Knokke-Heist, which allowed me to conduct more exposure tests. Your ongoing assistance with the experiments has been greatly appreciated.

To my parents, **Ruihua Sun** and **Yuxia Li**, for their support and encouragement throughout my journey. You are my constant source of inspiration in life.

Lastly, I would like to extend a special thank you to my partner, **Yu Weng**. Your positivity and unwavering belief in me have been instrumental in the completion of this document, and I am truly grateful for your continuous support and love.

TABLE OF CONTENTS

LIST OF FIGURES

LIST OF TABLES

LIST OF ABBREVIATIONS

BM	. . . . .	Base Metal
CRC	. . . . .	Corrosion Resistance Class
CRF	. . . . .	Corrosion Resistance Factor
CS	. . . . .	Carbon Steel
DSS	. . . . .	Duplex Stainless Steel
EDS	. . . . .	Energy Dispersive Spectroscopy
GMAW	. . . . .	Gas Metal Arc Welding
HAZ	. . . . .	Heat-Affected Zone
IGC	. . . . .	Intergranular Corrosion
MAE	. . . . .	Mean Absolute Error
MSE	. . . . .	Mean Square Error
NPV	. . . . .	Net Present Value
PREN	. . . . .	Pitting Resistance Equivalent Number
R^2	. . . . .	R-Squared
RMSE	. . . . .	Root Mean Square Error
SCE	. . . . .	Saturated Calomel Electrode
SEM	. . . . .	Scanning Electron Microscope
SKW	. . . . .	Sint-Katelijne-Waver
WM	. . . . .	Weld Metal
XPS	. . . . .	Extruded Polystyrene

LIST OF SYMBOLS

Upper-Case Letters

A	.....	Area of the specimen	.....	[cm^2]
Al	.....	Aluminium	.....	[-]
C	.....	Carbon	.....	[-]
Cl^-	.....	Chloride ion	.....	[-]
Cr	.....	Chromium	.....	[-]
Cu	.....	Copper	.....	[-]
$F1$	.....	Risk of exposure to chloride from salt water or de-icing salts	.....	[-]
$F2$	.....	Risk of exposure to sulphur dioxide	.....	[-]
$F3$	.....	Cleaning regime or exposure to washing by rain	.....	[-]
Fe	.....	Iron	.....	[-]
Fe^{2+}	.....	Ferrous ion	.....	[-]
Fe_3O_4	.....	Iron oxide black	.....	[-]
$Fe(OH)_2$	.....	Iron (II) hydroxide	.....	[-]
$Fe(OH)_3$	.....	Iron (III) hydroxide	.....	[-]
$FeOOH$	.....	Ferric oxyhydroxide	.....	[-]
α-$FeOOH$	.....	Goethite	.....	[-]
γ-$FeOOH$	.....	Lepidocrocite	.....	[-]
$f(T)$	.....	Correction factor	.....	[-]
H^+	.....	Hydrogen ion	.....	[-]
H_2O	.....	Water	.....	[-]
I	.....	Welding current	.....	[A]
K	.....	Conversion factor = 8.76×10^7	.....	[-]
M	.....	Distance from the sea	.....	[km]
Mn	.....	Manganese	.....	[-]
Mo	.....	Molybdenum	.....	[-]
N	.....	Nitrogen	.....	[-]

Nb	Niobium	.....	[-]
Ni	Nickel	.....	[-]
O_2	Oxygen	.....	[-]
OH^-	Hydroxide	.....	[-]
P_d	Sulphur dioxide deposition rate	.....	[mg/(m²·d)]
Q	Heat input	.....	[kJ/mm]
R_{corr}	First-year corrosion rate	.....	[µm/a]
RH	Relative humidity	.....	[%]
S	Distance from roads with de-icing salts	.....	[km]
S_d	Chloride deposition rate	.....	[mg/(m²·d)]
Si	Silicon	.....	[-]
SO_2	Sulphur dioxide	.....	[-]
T	Temperature	.....	[°C]
Ti	Titanium	.....	[-]
U	Welding voltage	.....	[V]
V	Arc travel speed	.....	[cm/min]
W	Mass loss of the specimen	.....	[g]

Lower-Case Letters

a	Throat thickness	.....	[mm]
e^-	Electron	.....	[-]
f_i	The predicted value	.....	[-]
t	Exposure time of the specimen	.....	[h]
$\bar{t}$	Plate thickness	.....	[mm]
ρ	Density of the specimen	.....	[g/cm³]
τ	Time of wetness	.....	[h/a]
n	The number of data points	.....	[-]
$\bar{y}$	The mean value derived from the real-measured data	.....	[-]
y_i	The corresponding measured value	.....	[-]

1

Introduction

Dissimilar welds are increasingly used in engineering applications, especially are being applied to girder bridges in corrosive environments due to economic benefits. Hybrid solutions, combining carbon steel and stainless steel, have the potential to reduce lifecycle costs of a bridge. This reduction can be attributed to the decreased maintenance expenses associated with painting requirements as well as economic losses that arise from possible traffic closures [2]. Bouassida et al. [3] concluded that incorporating stainless steel components offered an advantageous position in terms of the net value of lifecycle costs when compared to options involving painted carbon steel. A case study by Sterckx et al. [4] demonstrated that the total net present value (NPV) of a girder bridge using carbon steel S355J2 and duplex grade EN1.4062 was lower than for a bridge with fully made of stainless steel. Another case study by Karabulut et al. [5] addressed that, in a hybrid girder bridge, partially replacing S355J2 carbon steel with EN1.4162 duplex can lead to both weight reduction and lower maintenance costs. In addition to cost benefits, it is important to consider that certain components of a bridge may be difficult to access and maintain due to their location or structural design. To address this challenge, the parts that are hard to reach are manufactured using stainless steel, while the parts that are easily repainted for maintenance purpose can be constructed using carbon steel [2]. For example, in a paper by Yabuki et al. [6], a

box-girder bridge was studied where stainless steel duplex grade was used in the webs of the girders and carbon steel was used for the stiffeners. Thus, combining carbon steel and stainless steel allows to keep overall costs lower while increasing the corrosion resistance only where it is truly needed.

However, a lot of complexities are encountered in structures with dissimilar welds such as compositional gradients resulting from the differences in chemical compositions which may result in the migration of carbon element from the higher carbon containing alloy to the relatively lower one [7-10]. Carbides precipitation, such as the formation of chromium carbide, is also observed in the heat-affected zone of stainless steel, diminishing the chromium content in the area nearby the grain boundary and also leaving the area around the grain boundary more susceptible to corrosion [11, 12]. Microstructural changes in dissimilar welds have also been widely reported [13-17]. These compositional gradients and microstructural changes may lead to large variations in corrosion properties across the welds, causing deterioration of the corrosion protection supplied by the surface passive film and making it crucial to keep a critical eye on the corrosion behaviour of the welds [18-20]. Moreover, if the welding process is not adequately controlled, some welding-induced imperfections such as dilutions, cracks and residual stresses can occur both in the weld nugget and the heat-affected zone [14, 21, 22].

The literature on the corrosion behaviour of common grades of stainless steels and carbon steels is rather rich, however, there is limited information about the corrosion resistance of dissimilar welds, especially on welds between duplex stainless steels and carbon steels [18, 21, 23]. To support a wider the use of these dissimilar welds in civil construction where superior corrosion resistance is only needed in certain areas, a better understanding of the corrosion behaviour under different corrosive environments is key. This is the topic investigated in this paper.

2

Background

2.1 Overview of studied materials

2.1.1 Carbon steel

Carbon steel is an alloy of iron, carbon (≤2%), and other alloying elements [24]. Two carbon steels are considered in this study: the European Standard structural steel S355J2 which has a minimum yield strength of 355 MPa, as well as P460NL2 steel, a high-quality pressure vessel steel grade with a minimum yield strength of 460 MPa. The studied carbon steel grades are both low-carbon, medium tensile and readily weldable materials, and are increasingly employed in bridge constructions. The stress-strain curves for the used grades[1] are shown in Figure 2-1. The (maximum) chemical composition of carbon steels S355J2 and P460NL2 are given in Table 2-1, according to EN 10025-2 [25] and EN 10025-3 [26].

Table 2-1. Chemical composition (maximum) of the studied carbon steel grades [25, 26].

Grade	Chemical composition [wt.%]						
	C	*Si*	*Mn*	*Cr*	*Ni*	*Mo*	*Cu*
S355J2	≤0.20	≤0.55	≤1.60	-	-	-	≤0.55
P460NL2	≤0.20	≤0.60	1.10 - 1.70	≤0.30	≤0.80	≤0.10	≤0.70

[1] The duplex stainless steel grade EN1.4062 will be described in the next section.

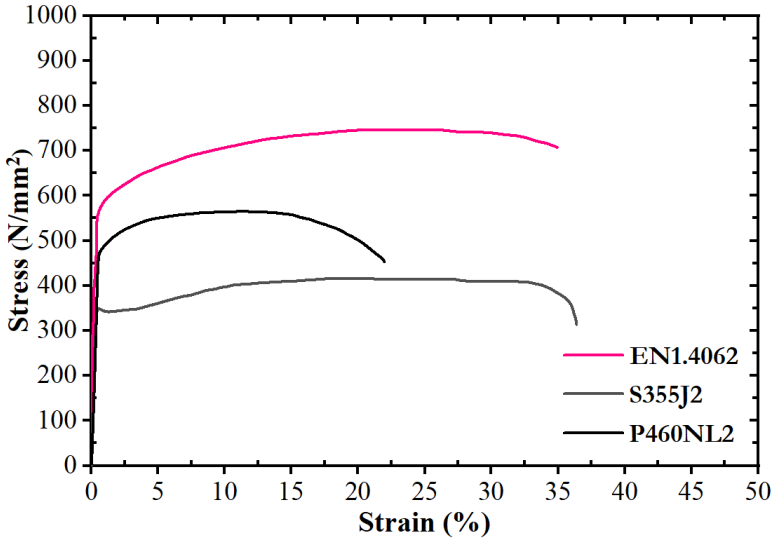

Figure 2-1. Stress-strain curve for all studied grades, adapted from [5, 27].

2.1.2 Stainless steel

Stainless steels are alloys that contain a minimum of 10.5% of chromium and a maximum of 1.2% of carbon in mass [28]. Stainless steels show good to excellent corrosion resistance when exposed to aggressive environments, such as coastal areas or under the influence of de-icing salts [28]. Therefore, stainless steels are usually characterised by low to absolute zero maintenance costs. Stainless steel grades are categorised in four families, depending on their microstructure at room temperature, as the distinct microstructures result in unique properties and different corrosion resistance classes. Most commonly used families in structures are the austenitic, and duplex ones. Austenitic and duplex stainless steels are characterised by a wide range of mechanical strengths in service temperatures which make them ideal in structural applications.

Austenitic stainless steels are the most commonly used grades in construction and are known to combine excellent corrosion resistance with high ductility. Duplex stainless steels are characterised by a balanced austenitic-ferritic microstructure. The austenite phase is distributed uniformly in the ferrite matrix like islands in

morphology, usually elongated along the rolling direction. Duplex stainless steels are ideal when very high strength and excellent corrosion resistance are of primary importance [29-31]. Within the duplex family, lean duplex grades (e.g., EN1.4062) are typically used for structural applications in medium corrosive environments ($-15<CRF^{2}\leq-7$) when higher strength is required, i.e., where austenitic grades cannot meet this criterion [32]; standard duplex grades have high corrosion resistance and are applicable in aggressive environments ($-20\leq CRF\leq-15$) such as coastal ones [28]; super duplex grades, which have very high corrosion resistance, meet the demands for very aggressive environments ($CRF<-20$), i.e., offshore areas with high salinity or industrial areas with aggressive atmosphere and extreme humidity or subtropical and tropical atmospheres, according to the standard ISO 12944-2 [33].

The lean duplex grade EN1.4062 has economic advantage compared to conventional duplex (e.g., EN1.4462) due to the lower content of molybdenum and nickel. EN1.4062 has similar corrosion resistance to the standard austenitic grades EN1.4307 and EN1.4404 with superior yield strength and ultimate elongation capacity [34-38]. In medium corrosive environments, EN1.4062 offers a cost-effective and performance-efficient alternative to more costly conventional duplex or austenitic grades.

2.2 Dissimilar welding

Welding between dissimilar metals is commonly called dissimilar welding. Dissimilar welding is gaining more and more interest owing to previously mentioned cost-benefit performance of dissimilar welding in various applications.

[2] The Corrosion Resistance Factor (CRF) will be described in Chapter 3.

2.2.1 Typical zones of a weld

A weld has three typical zones: weld metal (WM), the heat-affected zone (HAZ) and base metal (BM) (Figure 2-2). Weld metal is the metal which has been molten in the welding process and then solidified [39]. It is generally a mixture of filler metal and base metal, and has an inhomogeneous metallurgical structure because of the percent dilution of base metal which is highest near the fusion boundary and gradually decreases away from it [39, 40]. The heat-affected zone lays between fusion boundary and base metal. This zone experiences temperatures below the melting point, but significant enough to change the microstructure and hence the mechanical properties. The mechanical properties in the heat-affected zone are such that this region is usually a preferential site for failure. Base metal is the zone unaffected by heat where the initial microstructure is preserved.

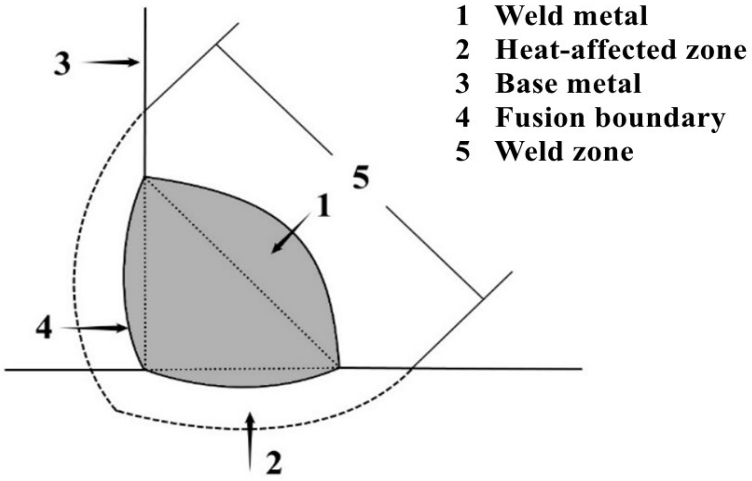

Figure 2-2. Schematic drawing of a fillet weld.

2.2.2 Selection of the welding process and filler metal

The selection of the welding process and filler metal for welding structural steel is the key to obtain high quality dissimilar welding [41]. When selecting a welding process, two primary factors take precedence: the cost and the capability to meet

design requirements [41]. In terms of the welding techniques, today's research mainly focusses on solid-state welding and fusion welding [42]. Among the solid-state techniques, diffusion bonding, explosive welding and friction stir welding are most commonly reported [42-44]. In the fusion welding category, beam-assisted technique and arc welding are the most studied processes [45]. Gas metal arc welding (GMAW) is a widespread fusion welding method to weld dissimilar metals and results in high-quality spatter-free welds with low distortion [45]. GMAW process has been employed in this study to weld duplex stainless steel to carbon steel thanks to its adaptability to mass production and relatively low cost [41].

The selection of filler metal largely depends on the chemical composition of welding materials. In dissimilar welding of carbon steel and duplex stainless steel, stainless steel rather than carbon steel is generally selected as the filler metal in order to avoid dilution of the alloying elements near the fusion boundary of the duplex grade [46, 47]. A percentage between 2% and 10% of ferrite in the weld metal is desirable to avoid hot cracks [41]. Schaeffler diagram is a widely employed tool in the selection of suitable filler metals [41]. Originally introduced in 1948 to estimate the ferrite content in austenitic stainless steels, this diagram has evolved to encompass the prediction of ferrite content in dissimilar welds [48]. Chromium-equivalent and nickel-equivalent, which reflect the influence of the ferrite and the austenite stabilizing elements on the resulting structure, are calculated from the chemical composition, using the formula provided in abscissa and ordinate (see Figure 2-3). Austenitic stainless steel wire (e.g., 309LSi) can provide a proper austenitic microstructure with sufficient ferrite content (>6%) and hence is used in dissimilar welding of duplex stainless steel (EN1.4062) to carbon steels (S355J2 and P460NL2) [49]. Austenitic stainless steel wire 309LSi can also be alloyed with chromium to compensate for any chromium losses that may occur during the welding process [2]. Moreover, it is a common practice to aim for superior

mechanical properties in the weld metal compared to those of the base metal, as this is crucial for maintaining structural integrity [50, 51]. In this project, tensile tests revealed that the weld exhibited a strength that surpassed that of both base metals, indicating overmatching [2].

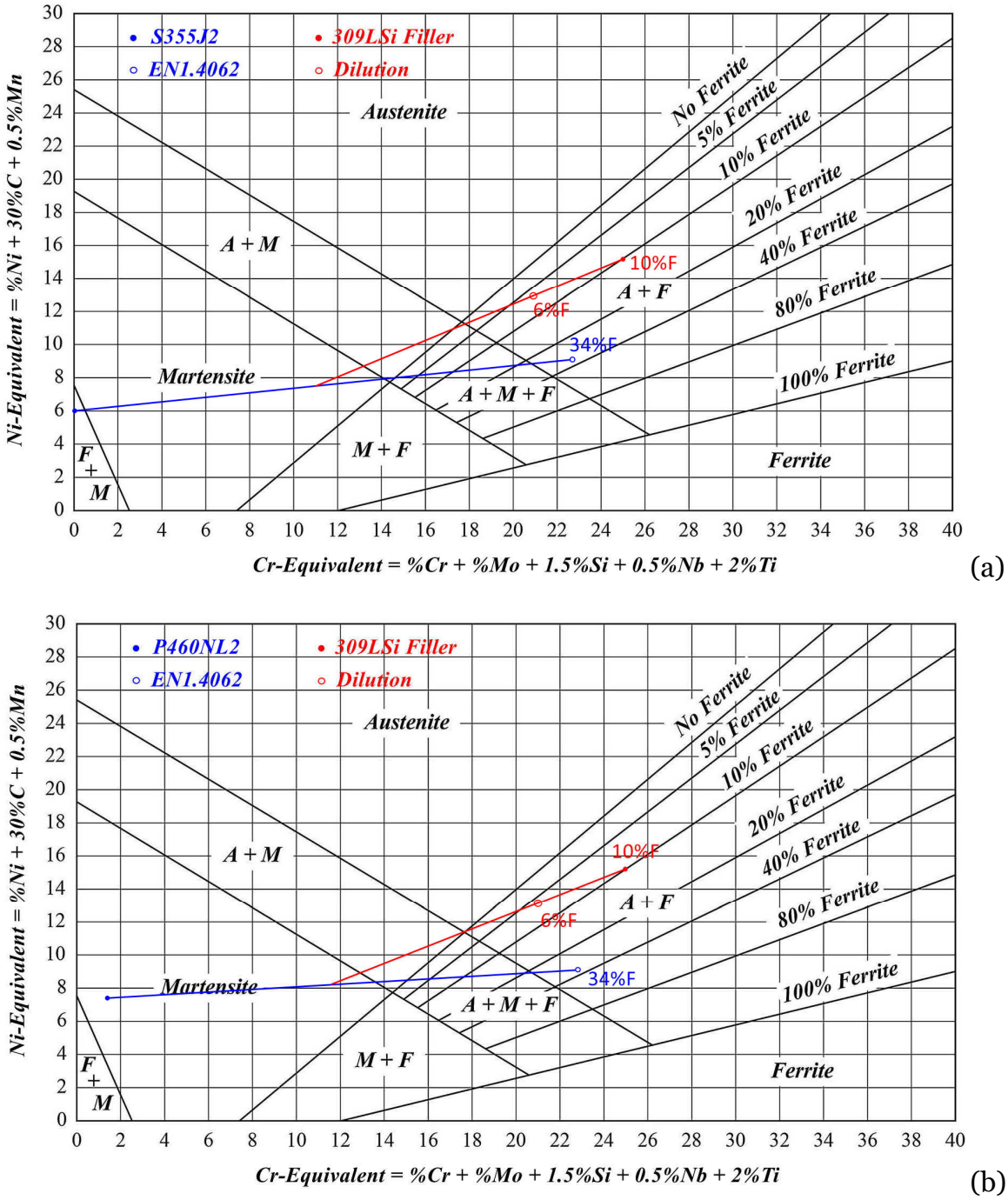

Figure 2-3. Schaeffler diagram incorporating 309LSi as filler metal for EN1.4062 and (a) S355J2 or (b) P460NL2 as base metals.

2.2.3 Microstructure of dissimilar carbon-duplex stainless steel welds

During welding, the microstructure in the vicinity of the welding metals undergoes transformations. The microstructure of weld zone is influenced by solidification rate, heat input, and welding materials [52]. Microstructural examinations reveal that the high temperature followed by cooling at high rate leads to modification of the proportion of ferrite and austenite in the microstructure of the HAZ of stainless steel which can significantly alter the mechanical characteristics [53]. Martensite can also appear at the boundaries of the ferrite grain in the HAZ due to the formation of austenite at these grain boundaries at high temperatures and its subsequent transformation to martensite because of high cooling rate [14, 52]. Barnhouse & Lippold [54] have reported that heat input level affects precipitation of chromium nitride from the grain boundaries in the ferrite phase and formation of secondary austenite. These changes in the original volume percentage of ferrite and austenite have subsequent adverse effects on the mechanical properties and corrosion resistance of the material [54, 55]. For instance, the increased volume fraction of ferrite can decrease the hardness of duplex stainless steel [55].

Using an austenitic filler metal 309LSi which contains approximately 10% ferrite, Cools & Staepels [2] have observed different microstructures in the weld zone of carbon steel. Though the same electrode is used, the morphologies of ferrite and austenite phases in the weld metal of S355J2 and P460NL2 appear different, as shown in Figure 2-4. More specifically, an δ-ferrite in the form of skeletal ferrite morphology is seen in the weld metal of S355J2, which is known to have excellent fatigue-resistance due to an interlocking effect of fine grain size [2, 41, 56]. Whereas, an almost continuous δ-ferrite network in an austenitic matrix is seen in the weld metal of P460NL2 [57]. The type of discontinuous interface, Type II

boundary, is observed between weld metal and carbon steel base metal in the microstructure (Figure 2-5), which indicates that crystal structures between filler metal and carbon steel are dissimilar [19]. The grain sizes of the HAZ of carbon steel also change significantly. Starting from the weld metal, a coarse-grained area is followed by a transition area with fine grains [2]. The grain size plays a significant role on the fatigue resistance, as an increase in grain size decreases the resistance of the grain boundaries to crack propagation [58]. In the coarse-grained section, fatigue damage predominantly transpires through the formation of slip bands followed by subsequent crack propagation along these slip bands and grain boundaries [58]. Conversely, in the fine-grained region, fatigue damage primarily occurs through cracking along the grain boundaries.

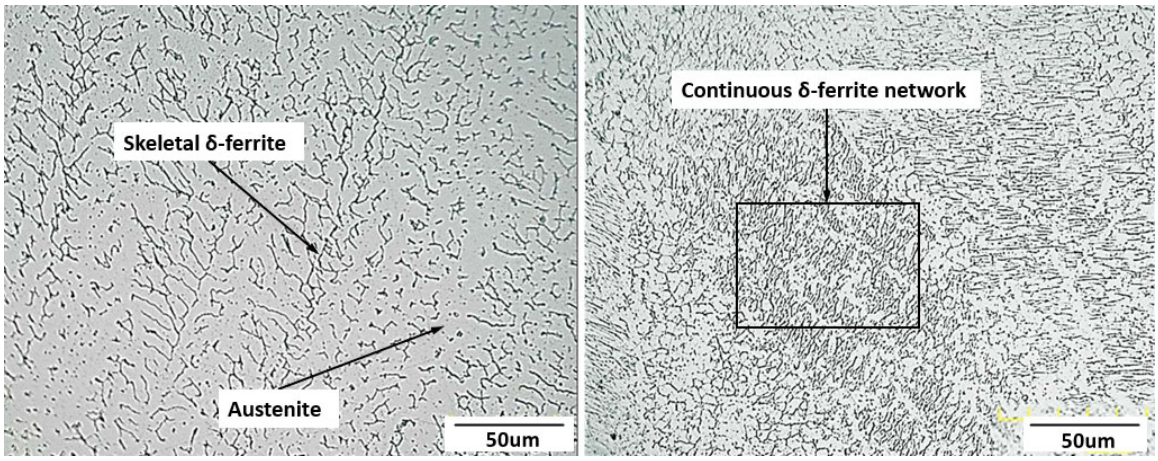

Figure 2-4. Microstructure in the weld metal - S355J2 (left) and P460NL2 (right), magnification 50 μm [2].

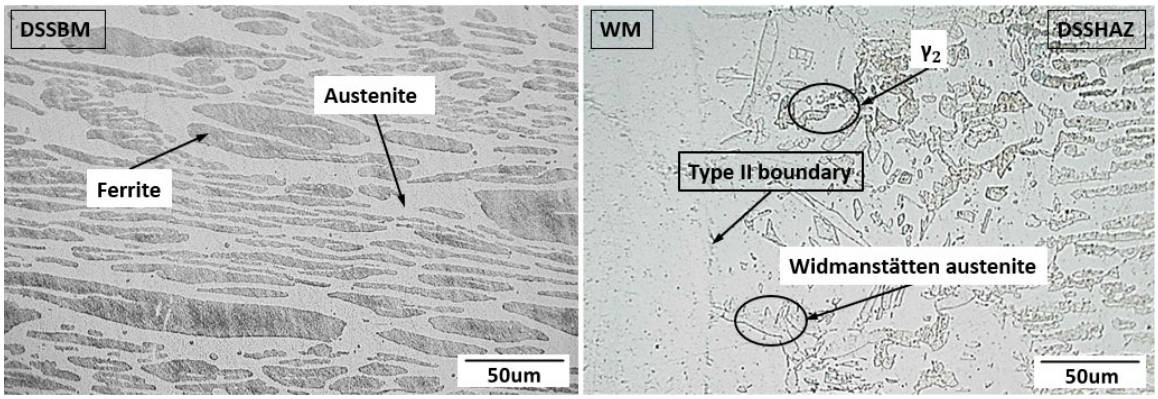

Figure 2-5. Microstructure in duplex stainless steel EN1.4062 - Base metal (left) and the HAZ (right), magnification 50 μm [2].

2.2.4 Defects

2.2.4.1 Crack

Crack is the most severe weld defect and can be categorised as typical cracks in the dissimilar welding, i.e., (a) tee cracks which can occur in the weld or the HAZ [10], and (b) cold and hot cracking which can affect the weldability of carbon steel and stainless steel, respectively [59]. The austenitic solidification mode and the brittle martensite formation caused by element diffusion along with further metallurgical changes are the main causes of cracks in dissimilar welded joints [60, 61]. Furthermore, microcracks are formed during the solidification process due to the variation of stresses in the cooling phase [62]. However, cracks in dissimilar welded joints can be controlled via proper selection of welding parameters and filler metal [63, 64].

2.2.4.2 Carbon migration

Carbon steel generally contains a higher carbon content compared to stainless steel, and this chemical gradient has the potential to induce carbon diffusion from carbon steel to stainless steel [2]. Carbon migration results in grain growth and

decarburization in the heat-affected zone of carbon steel, resulting in a reduction of mechanical properties [2]. Furthermore, it causes carburization of the weld zone in the vicinity of the stainless steel grade [2]. This can allow carbides to form which can greatly increase hardness and cracking susceptibility [11, 12].

2.2.4.3 Residual stress

The efficiency of residual stress relief in dissimilar joints is lower than that of non-dissimilar ones, due to greater relative thermal expansion of the welding metals [9, 10]. This may lead to a dramatic shift in the composition nearby the fusion boundary and degradation of the mechanical properties [8].

2.3 Corrosion

2.3.1 Atmospheric corrosion process

Atmospheric corrosion is a complex process. Generally, the key environmental factors can be categorised into two groups: climate factors (e.g., time of wetness, humidity, temperature, and rainfall) and pollutants or salts in the air, which can affect corrosion simultaneously [65]. In light of this complexity, field exposure test is the most reliable method to study natural atmospheric corrosion behaviours [66].

Atmospheric corrosion takes place when a layer of electrolyte forms on the surface of a metal [67]. The formation of this layer is primarily influenced by variations in the temperature and atmospheric humidity [67]. In the initial stage, droplets fall on steel surface to form a thin aqueous film rapidly, especially when pollutants exist in the atmosphere, which can result in the localized dissolution of the oxide film on the surface [65]. In terms of pollutants in the air, the deposition of sulphur dioxide is of key importance to corrosion [66]. Sulphur dioxide is produced from

several sources, including combustion processes of low-grade fuels and other industrial activities. It not only participates in the corrosion process, but also generates an acidic liquid on the steel surface, accelerating atmospheric corrosion of steel [68]. The primary source of salts in the air is the ocean. Sea wind normally carries an average of 10 lbs to 100 lbs of sea-salt per cubic mile of air [69]. Wessenrieder & Leygral [70] observed that the nucleation of the initial corrosion product occurred at droplets of sodium chloride. Preston & Sanyal [71] also reported that the presence of sodium chloride played a significant role in the nucleation of corrosion on steel. Therefore, the complex interplay between the key environmental factors has been demonstrated to be an important factor to drive the atmospheric corrosion [67].

2.3.2 Types of corrosion

Under atmospheric conditions, steel commonly experiences various types of corrosion. However, this study specifically focusses on three predominant corrosion types, i.e., uniform corrosion, pitting corrosion, and galvanic corrosion.

2.3.2.1 Uniform corrosion

Uniform corrosion occurs on the steel surface at a predictable constant rate which is represented as a thickness reduction over time. During uniform corrosion, steel is removed uniformly from the exposed surface [72].

2.3.2.2 Pitting corrosion

Pitting corrosion is a form of localised corrosion that leads to the formation of pits on the metal surface. It is primarily caused by chloride ions, although other halides and anions can have similar effects [28]. The extent of pitting is usually superficial, resulting in negligible reduction in the section of a component [28]. However, pitting corrosion can be more destructive compared to uniform corrosion, as it is

difficult to predict, detect, and design against [32].

2.3.2.3 Galvanic corrosion

Galvanic corrosion is an electrochemical process that happens when two dissimilar metals are connected in a corrosive electrolyte [72, 73]. In a bimetallic couple, the less noble material assumes the role of the anode and is prone to corrode at an accelerated rate [74]. Stainless steels are more noble than most metallic materials in most environments, thus galvanic corrosion is likely to affect metals in contact with stainless steel, such as carbon steels.

Galvanic series of metals based on experiments in seawater is frequently used to assess the prevalence of galvanic effects, as shown in Figure 2-6 [74]. In a galvanic couple comprising any two metals from the galvanic series, the corrosion of the metal positioned higher in the list is prone to be accelerated [74]. To assess the electrochemical behaviour of the studied materials further, both carbon steel S355J2 and duplex grade EN1.4062 were placed in 1M sodium chloride solution for 12 hours and the potential differences were recorded continuously. It was observed that the mean value of potential difference measurements was +0.41 V, as introduced in Figure 2-6. This observation clearly brings out that EN1.4062 is the nobler material. Therefore, galvanic corrosion of S355J2 could occur spontaneously in the right environment. Moreover, carbon steel P460NL2 shows similar electrochemical behaviour to S355J2 and therefore the same conclusion can be drawn.

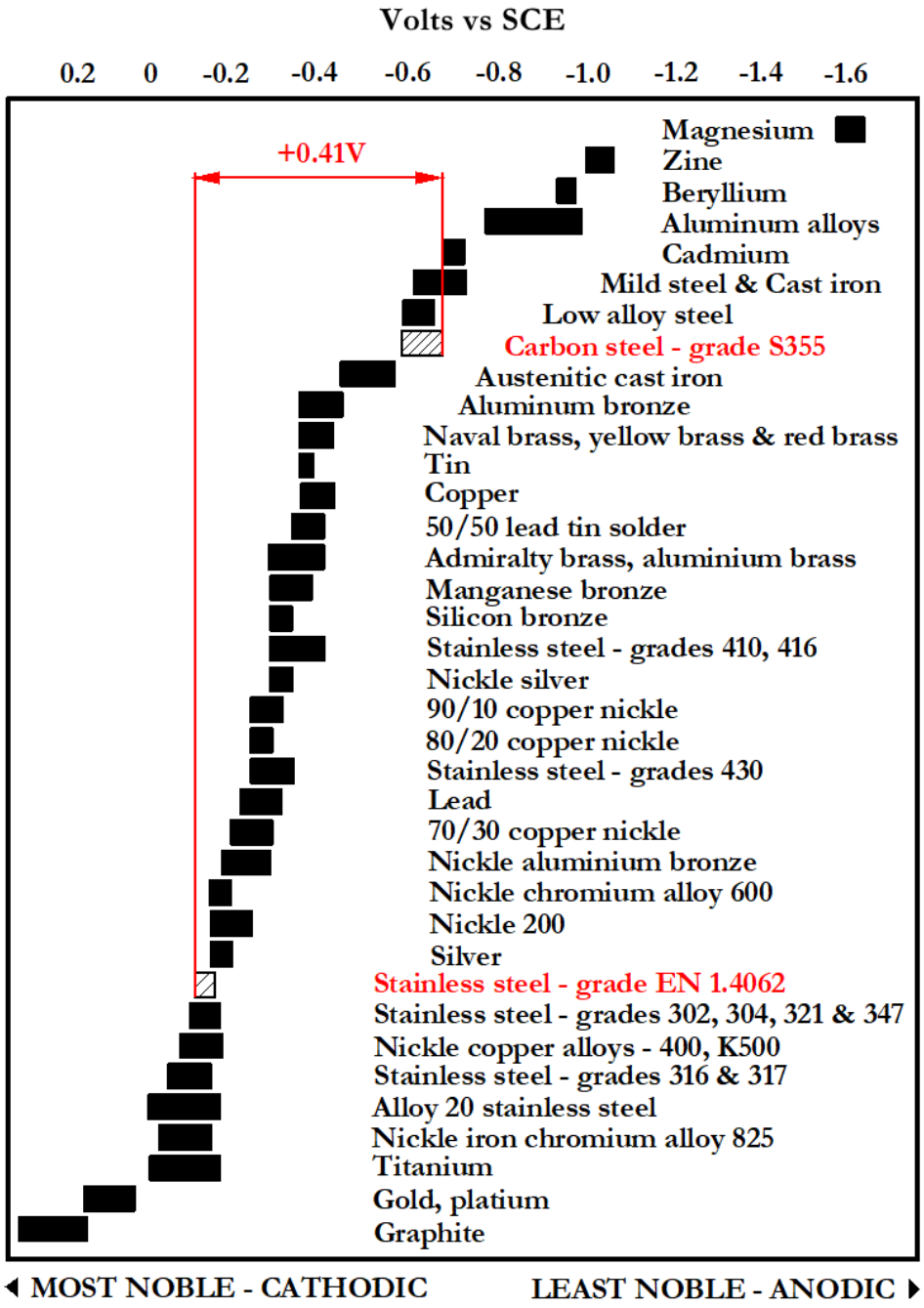

Figure 2-6. Galvanic series in seawater including new test (dashed lines), adapted from [74].

2.3.3 Corrosion performance of steels

2.3.3.1 Carbon steel

In the initial stage of atmospheric corrosion, uniform corrosion is prominent on

the surface of carbon steel. The rust formed on the surface consists of various oxides, including miscellaneous crystalline compounds, oxyhydroxides, hydrated oxides, and other compounds formed as a result of the reaction between iron and its surrounding [75]. The main electrochemical reactions in the initial stage can be described as follows (see Equation 2-1 to 2-2).

$$Fe \rightarrow Fe^{2+} + 2e^{-} \quad 2\text{-}1$$

$$O_2 + 2H_2O + 4e^{-} \rightarrow 4OH^{-} \quad 2\text{-}2$$

The dissolved Fe^{2+} combines with OH^{-} to form $Fe(OH)_2$ which may be further oxidized to the oxyhydroxides such as $FeOOH$ and $Fe(OH)_3$ [67]. It is a consensus that crystalline lepidocrocite (γ-$FeOOH$) is the initial phase to form on the steel surface [75, 76]. As the exposure time extends and the rust layer thickens, the active γ-$FeOOH$ undergoes partial transformation into inactive goethite α-$FeOOH$. This results in the formation of a dual rust layer consisting of a porous outer layer of γ-$FeOOH$ and a more compact inner layer of α-$FeOOH$ [75]. The reactions can be written as follows (see Equation 2-3 to 2-5).

$$3\gamma\text{-}FeOOH + H^{+} + e^{-} \rightarrow Fe_3O_4 + 2H_2O \quad 2\text{-}3$$

$$Fe^{2+} + 2\gamma\text{-}FeOOH \rightarrow Fe_3O_4 + 2H^{+} \quad 2\text{-}4$$

$$4Fe_3O_4 + O_2 + 6H_2O \rightarrow 12\alpha\text{-}FeOOH \quad 2\text{-}5$$

Localized corrosion is another main characteristic on carbon steel surface in the initial stage of corrosion under atmospheric exposure test conditions. Pits and surface defects are generally the initial centre of localized corrosion before the rust layer forms [68].

2.3.3.2 Duplex stainless steel

The corrosion resistance of stainless steel is provided by a thin passive film (1-3 nm) that forms on its surface in environments allowing oxidization [72]. The

chromium-rich oxides and hydroxides form this passive film which bonds very strongly to the metal surface and acts as a protective layer against the surrounding corrosive environment. However, in some extreme cases, pitting corrosion can affect stainless steel. Certain alloying elements are of great importance to secure the pitting corrosion resistance. The Pitting Resistance Equivalent Number (PREN) can be used as a rough estimation of the pitting resistance of stainless steel grades in a chloride-containing environment based on the alloying elements which contribute to corrosion resistance (see Equation 2-6), according to the Duplex Stainless Steel Brochure [32].

$$\mathrm{PREN} = \%\,Cr + 3.3 \times \%\,Mo + 16 \times \%\,N \qquad 2\text{-}6$$

Chromium and molybdenum, the ferrite-stabilizing alloying elements, take up an important role in pitting corrosion while also decreasing the propagation rate of possible pits [72]. Nitrogen is a strong austenite stabilizer and has a beneficial influence on the resistance to pitting corrosion, pit propagation and intergranular corrosion (IGC). In this research, lean duplex stainless steel grade EN1.4062 has superior pitting corrosion resistance; its PREN is 27.

2.3.3.3 (Dissimilar) welds

The weldment undergoes significant changes in microstructure during welding, e.g., the formation of dichromium nitride and intermetallic, leading to a great effect on their corrosion resistance. Dichromium nitride precipitates particularly within the ferrite grains or phase boundaries, decreasing the pitting resistance of welds [77]. This is attributed to adjacent depletion of chromium and nitrogen that leads to a local reduction of the PREN [72]. Compared to austenite phase, ferrite is a more susceptible phase, and thus pitting corrosion tends to propagate preferentially within the dichromium nitride centres of ferrite grains [78]. The most common intermetallic phase in stainless steel is σ-phase, which is known to

have a detrimental effect on corrosion resistance (e.g., intergranular, pitting, and crevice) [79]. However, heat treatment can dissolve the intermetallic phase into steel matrix and relieve the stresses produced during the hot rolling process [80].

Welding operations also play a significant role in the corrosion behaviours of the welded joint. The higher heat input generally gives superior weld quality, together with more austenite microstructures in the WM that can improve the corrosion resistance. Conversely, high-content ferrite microstructures within the HAZ and WM may form when heat input is too low, resulting in a reduction of pitting corrosion resistance [81]. The slow cooling rate promotes nucleation and growth of austenite and allows diffusion of ferrite-stabilizing elements (e.g., chromium and molybdenum) into the ferrite phase, increasing the resistance to localized corrosion of both the HAZ and WM [82]. Abioye et al. [83] also observed that the corrosion resistance of welded joints was enhanced with lower welding speed.

Overall, detailed information on the corrosion resistance of dissimilar welds between carbon steel and duplex stainless steels is rather limited [18, 20, 21, 23]. To the authors' best knowledge, only the conventional S32205 duplex grade was tested and no data on lean duplex grades is to be reported. Srinivasan et al. [23] studied S32205 grade welded to IS2062 by shielded metal arc welding, with E2209 and E309 electrodes. It was observed that the corrosion resistance was worse for S32205 base metal than for the weld metal due to higher ferrite content, promoting galvanic interactions within the steel matrix. In [20], Wang et al. investigated the corrosion of weldments between S32205 and 16MnR by gas tungsten arc welding, via electrochemical corrosion tests. It was observed that pits were initially formed in ferrite grains nearby the boundaries between ferrite and austenite due to electrochemical potential differences caused by the ratio of biphase, which propagate from ferrite to austenite. Wang et al. [21] also studied dissimilar welds

between S32205 and low alloy steel and found galvanic corrosion between the latter and the weld metal. Luchtenberg et al. [18] studied the corrosion behaviour of welded joints between S32205 and ASTM A516 Grade 60 by GMAW process, via electrochemical corrosion tests. The formation of secondary austenite at the austenite-ferrite interface as well as Widmanstätten austenite characterised by low chromium, nitrogen, and molybdenum reduced corrosion resistance.

3

Experimental Setup and Exposure Programme

3.1 Test sites

The aggressivity of the environments can be classified according to a corrosion resistance factor (CRF[3]), a parameter dependent on the distance to the sea or roads with de-icing salts, sulphur dioxide (SO_2) concentration and specified cleaning regime [84]. The CRF value is inversely proportional to the corrosivity of the studied environment. In this study, atmospheric corrosion was investigated in four typical environments whose CRF are from -3 (low corrosivity) to -7 (medium corrosivity). A list of the sites together with the calculation of their CRF is given in Table 3-1. All test sites are located near the meteorological stations of each city. Figure 3-1 to Figure 3-4 describe the maps with distance from the sea and from the roads with de-icing salts for each site.

[3] Determination of CRF (CRF = $F1 + F2 + F3$) will be shown in Table A in APPENDIX A.

Table 3-1. Corrosion Resistance Factor (CRF) for each site [84].

Test site	CRF = *F*1+*F*2+*F*3	*F*1	*F*2	*F*3
Sint-Katelijne-Waver (SKW), Belgium	-3 (low corrosivity)	-3	0	0
Oxford, the United Kingdom	-3 (low corrosivity)	-3	0	0
Casalinho da Foz, Portugal	-3 (low corrosivity)	-3	0	0
Knokke-Heist, Belgium	-7 (medium corrosivity)	-7	0	0

Figure 3-1. Map of Sint-Katelijne-Waver, Belgium (distance from the sea = 40.9 km) (left); Exposure site (0.01 km < distance from the roads with de-icing salts ≤ 0.1 km) (right).

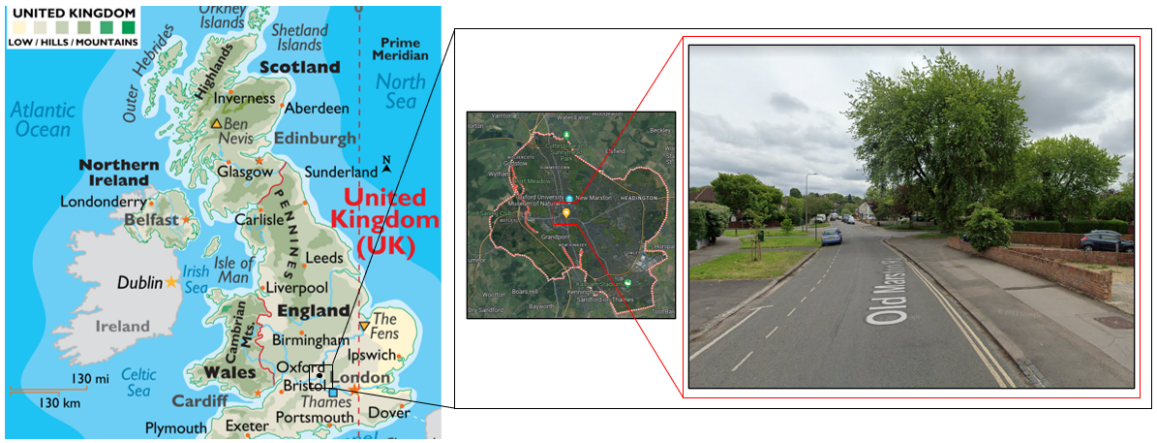

Figure 3-2. Map of Oxford, the United Kingdom (distance from the sea = 96.5 km) (left); Exposure site (0.01 km < distance from the roads with de-icing salts ≤ 0.1 km) (right).

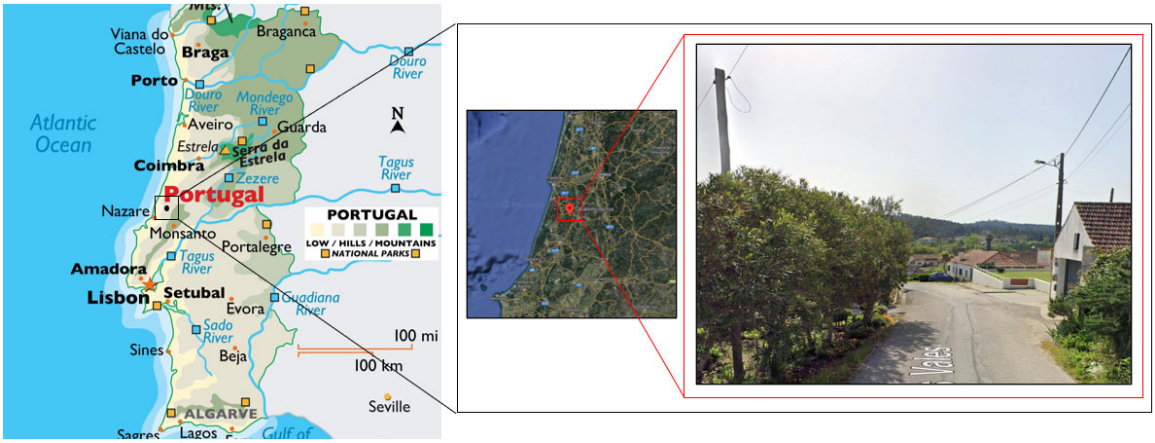

Figure 3-3. Map of Casalinho da Foz, Portugal (distance from the sea = 18.8 km) (left); Exposure site (0.01 km < distance from the roads with de-icing salts ≤ 0.1 km) (right).

Figure 3-4. Map of Knokke-Heist, Belgium (distance from the sea = 0.8 km) (left); Exposure site (0.01 km < distance from the roads with de-icing salts ≤ 0.1 km) (right).

3.2 Material selection

The Design Manual for Structural Stainless Steel [28] and the most recent provisions of the Eurocode 3 Part 1-4 [84] offer a method to select the most suitable stainless steel grade depending on the Corrosion Resistance Class (CRC). The CRC varies from I (very low resistance) to V (very high resistance). Table 3-2 gives the correlation between CRF and CRC [28]. Table 3-3 shows the grades of stainless steel in each CRC [28]. For the chosen four test sites, characterised by

low-corrosivity environment (CRF = -3) and medium-corrosivity environment (CRF = -7), a material should be selected from CRC III, e.g., lean duplex EN1.4062. In this study, one lean duplex stainless steel EN1.4062 and two carbon steels, S355J2 and P460NL2, were selected as the base materials.

Table 3-2. Correlation between CRF and CRC [28].

Corrosion Resistance Factor (CRF)	Corrosion Resistance Class (CRC)
CRF = 1 (very low aggressivity)	I (very low resistance)
-7 < CRF ≤ 0 (low aggressivity)	II (low resistance)
-15 < CRF ≤ -7 (medium aggressivity)	III (medium resistance)
-20 ≤ CRF ≤ -15 (high aggressivity)	IV (high resistance)
CRF < -20 (very high aggressivity)	V (very high resistance)

Table 3-3. Grades of stainless steel in each Corrosion Resistance Class (CRC) [28].

CRC	I (very low)	II (low)	III (medium)	IV (high)	V (very high)
Grades	1.4003	1.4301	1.4401	1.4439	1.4565
	1.4016	1.4307	1.4404	1.4462	1.4529
	1.4512	1.4311	1.4435	1.4539	1.4547
		1.4541	1.4571		1.4410
		1.4318	1.4162		1.4501
		1.4306	1.4662		1.4507
		1.4567	1.4362		
		1.4482	1.4062		

3.3 Sample preparation

Seven types of configurations were investigated in this study, as shown in Figure 3-5. The first three columns (a-c) are attributed to reference specimens, i.e., the base materials without welding. The welded T-joints are made by means of GMAW. The consumable used to fabricate the dissimilar welds is a 309LSi electrode with a diameter of 1 mm solid wire. Optimum welding parameters are selected according to Cools & Staepels [2], as shown in Table 3-4. Wide duplex plates ($\bar{t}_1$=12.5 mm)

are welded to the two chosen carbon steel plates, S355J2 ($\bar{t}_2$ =12 mm) and P460NL2 ($\bar{t}_3$=9 mm), by fillet welds (a=5 mm) from both sides, to form T-joints (d-e). The wider blocks are then segmented into specimens with thicknesses of 5 mm, considering the limitations imposed by the manufacturing equipment, which can ensure that the specimens survive the intended test period. The last two columns depict the welded joints which are only made of stainless steel, i.e., where carbon steel is removed (f-g). This is done to exclude the corrosion of carbon steel, to ease the comparison to the dissimilar T-joints.

Chemical compositions of the studied materials are provided by the manufacturer and are summarized in Table 3-5. The final specimens' dimensions are shown in Figure 3-6. Two holes are manufactured in each specimen to facilitate attachment to a test frame with rip-ties. For each specimen's type, three samples were fabricated [85]. Before exposure, abrasive blast cleaning was conducted in order to match the usual requirements for steel plates prescribed in bridge steelwork specifications [86], Sa2$^{1/2}$ surface quality, as well as to remove the weld notches.

Table 3-4. Used welding parameters for manufacture of the test samples [2].

Plate1	Plate2	Filler metal	Gas	Welding parameters			
				U [V]	*I* [A]	*V* [cm/min]	*Q* [kJ/mm]
EN1.4062	S355J2	309LSi	Arcal 129	27	253	45.2	0.73
EN1.4062	P460NL2	309LSi	Arcal 129	27	253	45.2	0.73

Where *U* is the welding voltage, *I* is the welding current, *V* is the arc travel speed and *Q* is the heat input.

Table 3-5. Chemical compositions of the studied grades.

Grade	Chemical composition [wt.%]							
	C	*Si*	*Mn*	*Cr*	*Ni*	*Mo*	*Cu*	*N*
EN1.4062	0.02	-	2.00	22.00	2.00	0.40	-	0.20
309LSi	0.02	0.80	1.80	23.50	13.50	-	-	-
S355J2	0.20	0.34	1.46	0.05	0.03	0.01	0.04	-
P460NL2	0.20	0.32	1.10	0.02	-	0.01	0.04	-

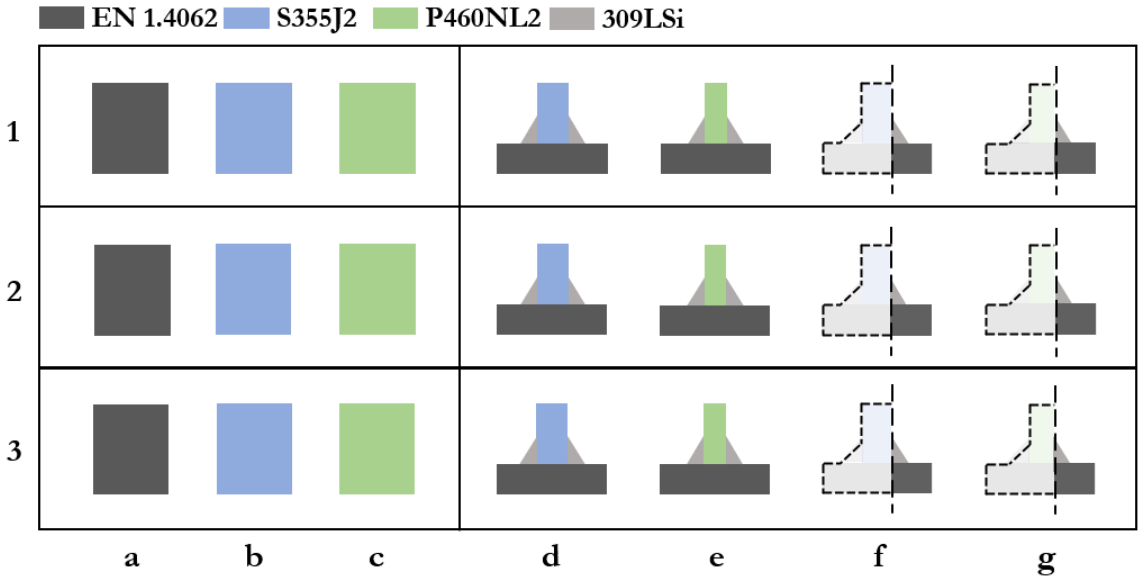

Figure 3-5. Schematic of the arrangement of the sample rack used for the exposure tests with: (a) EN1.4062 base plate; (b) S355J2 base plate; (c) P460NL2 base plate; (d) Dissimilar T-joint of EN1.4062/S355J2 with 309LSi electrode; (e) Dissimilar T-joint of EN1.4062/P460NL2 with 309LSi electrode; (f) Dissimilar weld of EN1.4062/309LSi (S355J2 removed); (g) Dissimilar weld of EN1.4062/309LSi (P460NL2 removed).

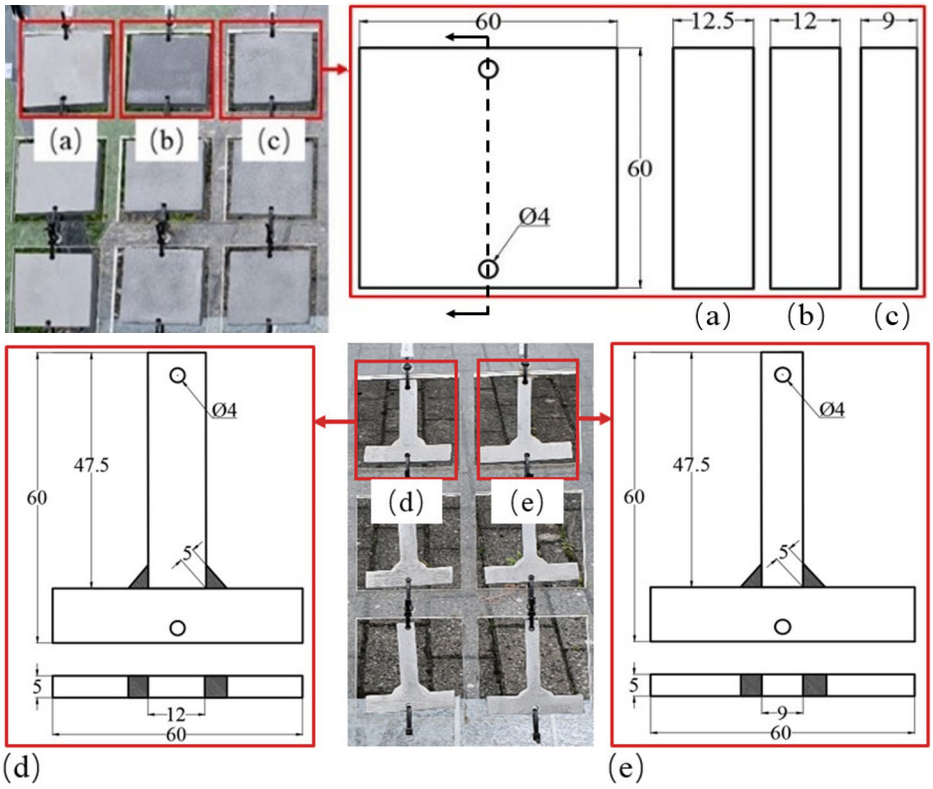

Figure 3-6. Scheme of welded specimens: (a) Geometry of EN1.4062; (b) Geometry of S355J2; (c) Geometry of P460NL2; (d) Geometry of T-joint: EN1.4062/S355J2/309LSi (electrode); (e) Geometry of T-joint: EN1.4062/P460NL2/309LSi (electrode).

3.4 Exposure programme

The exposure programme started in September 2021 and specimens were withdrawn after 12 months in August 2022. Pictures were taken on a regular basis (monthly). The test specimens were directly exposed, i.e., without any shelter. The height of the lowest samples was 75 cm above ground level, to prevent rain splashes [85]. The specimens were inclined at an angle of 45°, facing south, for maximum sunlight exposition (Figure 3-7).

The environmental parameters influencing the corrosion of dissimilar welds were monitored continuously at each test site (Figure 3-7). The devices used to collect the atmospheric information can be categorised as follows.

- Chloride measurements were performed using the 'dry plate' technique [87]. The chloride deposition was collected using a piece of dry gauze (100 mm × 100 mm) that was stretched and held in a Plexiglas frame, as shown in Figure 3-7(a). After monthly exposure, the gauze was washed, and the amount of deposited chloride was evaluated using ion chromatography. The gauze was sheltered to provide maximum protection from rain.
- The measurements of air temperature and relative humidity were recorded using an UX100-003 data logger (recording one point per hour), as shown in Figure 3-7(b). The logger was placed inside an extruded polystyrene (XPS) insulation box where the air flow was allowed from the sides and bottom while hindering the influence of radiation reflection from the metal surface below.

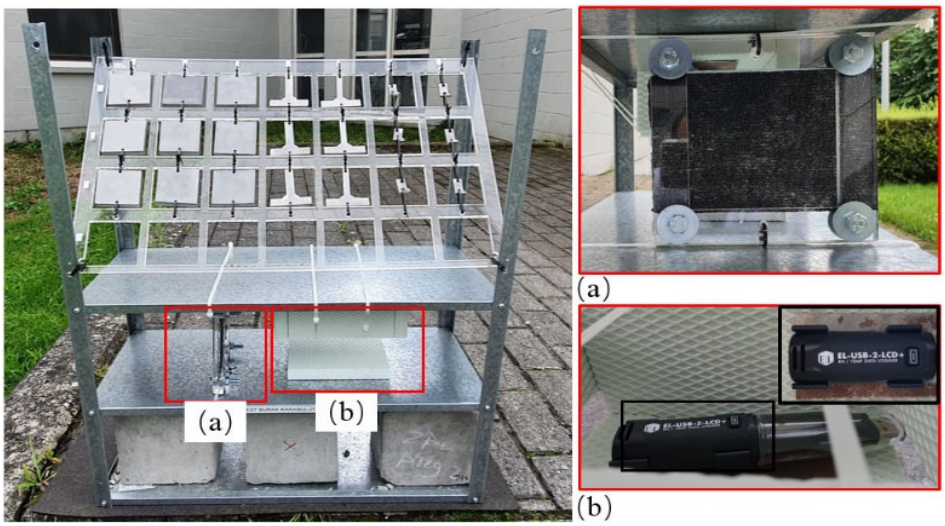

Figure 3-7. Photos of the devices used to collect: (a) Chloride deposition frame; (b) XPS insulation box for temperature/humidity sensor.

3.5 Post-corrosion examination

After one-year exposure, the samples were subjected to microscopic examination to examine the extent of corrosion using a Hirox KH-8700 digital microscope. The qualitative chemical analysis was conducted using a scanning electron microscope (SEM), equipped with an energy dispersive spectroscopy (EDS).

To calculate the corrosion rates by evaluating the mass loss, (loose) corrosion products should be removed in accordance with ASTM G1-90 [88]. The cleaning procedure should be repeated until weight loss stagnation. Afterwards, the cleaned specimens were weighed using a digital scale with an accuracy of ±0.001 g.

There is an error margin between the actual dimensions of each specimen and their ideal values due to manufacturing tolerances. To ensure precise measurement of the corrosion rates, it is necessary to account for the actual surface areas. In this study, the actual shape was mapped with AutoCAD (proportional scaling) and its surface precisely calculated for each specimen.

4

Long-Term Experimental Results

4.1 Environmental parameters

Environmental data are classified into different levels according to ISO 9223 [89], as outlined in Table 4-1. The standard describes four sulphur dioxide deposition rate categories from P0 to P3. The P3 level represents an industrial atmosphere characterised by high pollution, featuring the highest rate of sulphur deposition. Chloride deposition rate is also categorised into four levels, from S0 to S3, with S3 indicating the highest chloride deposition rate, ranging between 300 mg/(m^2·d) and 1500 mg/(m^2·d). The time of wetness refers to the duration during which the relative humidity exceeds 80% and the temperature remains above 0°C. The time of wetness is classified into five categories: at the τ1 level, material surface remains dry; at the τ2 level, a thin liquid film forms on the surface; and between τ3 and τ5, water films form, acting as electrolytes and promoting atmospheric corrosion of the material [90].

The monthly averages of humidity, temperature, sulphur dioxide deposition rate, chloride deposition rate, rainfall, and time of wetness for the period spanning September 2021 to August 2022 are illustrated in Figure 4-1. In this study, sulphur

dioxide deposition rates (P_d) and rainfall during the exposure time were not monitored and hence, these values were obtained from the European Environment Agency [91] and meteorological stations separately. The temperature exhibited a typically unimodal distribution over the year, with the inversion observed in January. Notably, Casalinho da Foz reported the highest monitored values of temperatures across all test sites, ranging from 9°C to 24°C. In contrast, the humidity level at each site remained relatively constant throughout the year. However, the humidity level in Sint-Katelijne-Waver experienced a slight decline from April to August, with values ranging from 59% to 62%. The deposition rates of sulphur dioxide at all test sites were below 4 mg/(m²·d), indicating a low level of pollution (P0 level). The test sites were in the level of S1 where the coastal city, Knokke-Heist, had the highest annual average chloride deposition rate of 17 mg/(m²·d). The time of wetness observed in this study ranged from 3349 h/a to 5030 h/a (τ4 level). This duration indicated the presence of water films, which act as electrolytes and contribute to the promotion of atmospheric corrosion of carbon steel. Moreover, the weather data (humidity and temperature) collected from the meteorological station during the exposure test period only has a small error range compared to the monitored values (Table 4-2). Hence, it sounds reasonable to collect data directly from the nearest meteorological station during the tests.

Table 4-1. Classification of the corrosivity of sulphur dioxide deposition rate, chloride deposition rate and time of wetness based on ISO 9223 [89].

Sulphur dioxide deposition rate		Chloride deposition rate		Time of wetness	
[mg/(m²·d)]	Level	[mg/(m²·d)]	Level	[h/a]	Level
$P_d \leq 4$	P0	$S_d \leq 3$	S0	$\tau \leq 10$	τ1
$4 < P_d \leq 24$	P1	$3 < S_d \leq 60$	S1	$10 < \tau \leq 250$	τ2
$24 < P_d \leq 80$	P2	$60 < S_d \leq 300$	S2	$250 < \tau \leq 2500$	τ3
$80 < P_d \leq 200$	P3	$300 < S_d \leq 1500$	S3	$2500 < \tau \leq 5500$	τ4
				$5500 < \tau$	τ5

Where the time of wetness is expressed in hours per year (h/a).

Table 4-2. Average humidity, average temperature, average sulphur dioxide deposition rate (P_d), average chloride deposition rate (S_d), rainfall and time of wetness at each site in 2021/2022.

Test site	Humidity [%]		Temperature [°C]		P_d [mg/(m²·d)]	S_d [mg/(m²·d)]
	Station	Monitored	Station	Monitored	Station	Monitored
SKW	71.5	73.0	14.0	13.2	1.2	8.0
Oxford	75.8	79.2	12.7	12.2	2.5	7.6
Casalinho da Foz	73.1	79.8	17.8	15.8	0.7	6.4
Knokke-Heist	73.9	75.5	13.6	13.0	1.2	17.0

(continued)

Test site	Rainfall [mm]	Time of wetness [h/a]
SKW	292	3721
Oxford	302	4991
Casalinho da Foz	280	5030
Knokke-Heist	163	3349

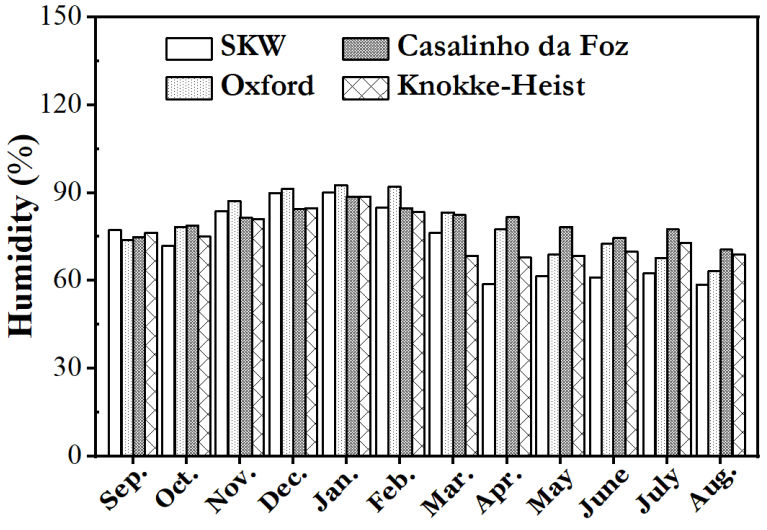

(a)

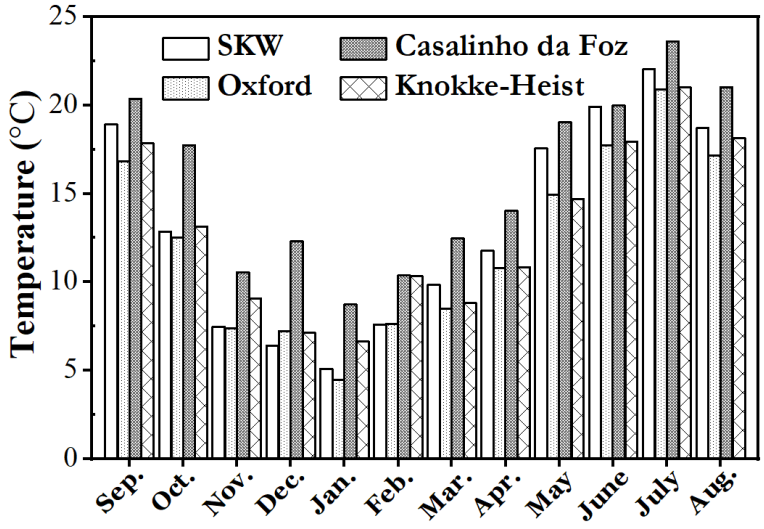

(b)

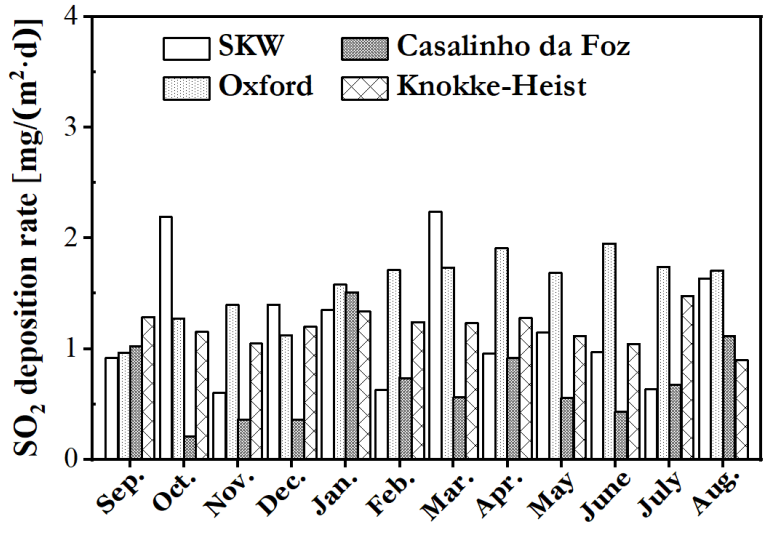
SKW
Casalinho da Foz
Oxford
Knokke-Heist
SO_2 deposition rate [mg/(m²·d)]
0
1
2
3
4
Sep.
Oct.
Nov.
Dec.
Jan.
Feb.
Mar.
Apr.
May
June
July
Aug.

(c)

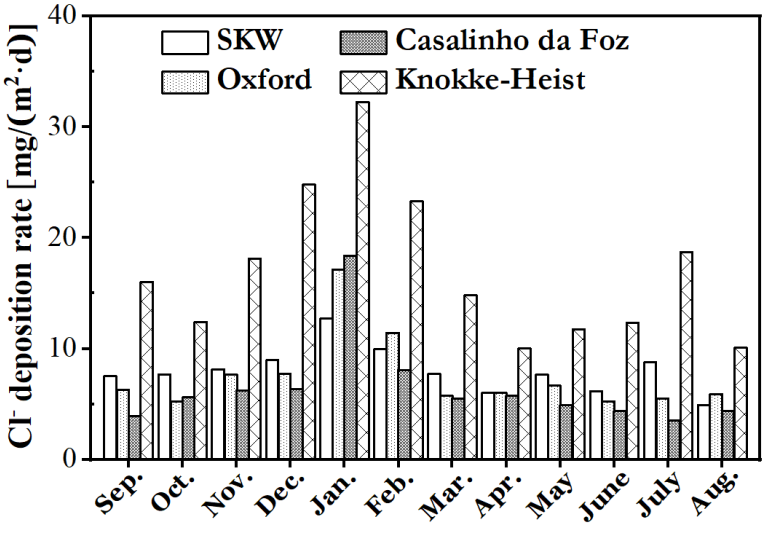
SKW
Casalinho da Foz
Oxford
Knokke-Heist
Cl^- deposition rate [mg/(m²·d)]
0
10
20
30
40
Sep.
Oct.
Nov.
Dec.
Jan.
Feb.
Mar.
Apr.
May
June
July
Aug.

(d)

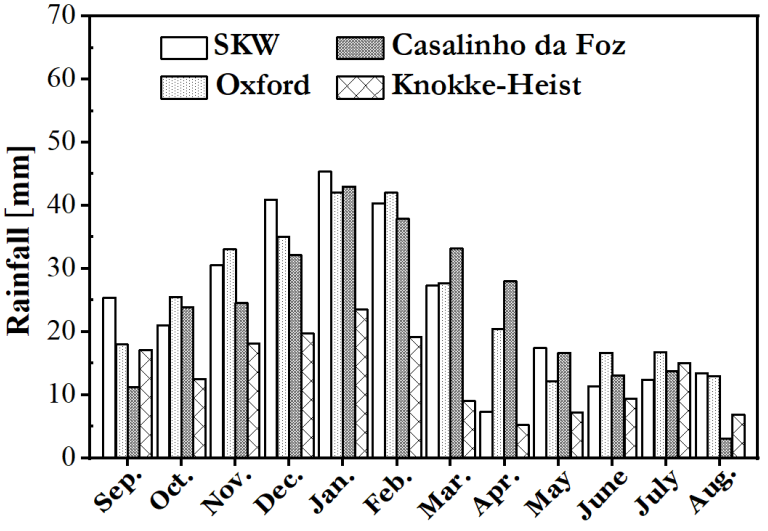
SKW
Casalinho da Foz
Oxford
Knokke-Heist
Rainfall [mm]
0
10
20
30
40
50
60
70
Sep.
Oct.
Nov.
Dec.
Jan.
Feb.
Mar.
Apr.
May
June
July
Aug.

(e)

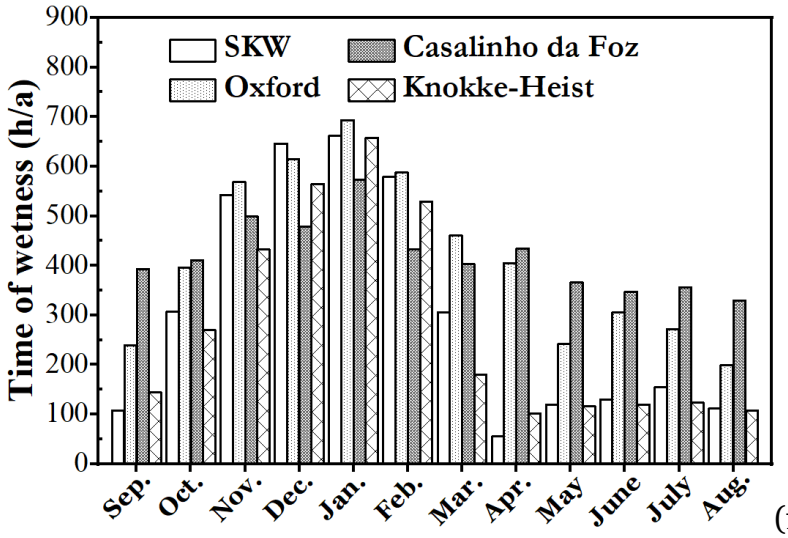

(f)

Figure 4-1. Monthly average values of (a) Humidity; (b) Temperature; (c) Sulphur dioxide deposition rate; (d) Chloride deposition rate; (e) Rainfall; (f) Time of wetness at each site from September 2021 to August 2022.

4.2 Morphology of the rust layer

During the exposure period, carbon steel plates S355J2 and P460NL2 showed different corrosion behaviours, as shown in Figure 4-2, taking Knokke-Heist as an example. In the initial stage, the rust layer on steel S355J2 was comparatively thinner than that on steel P460NL2. This can be explained when looking at their content of alloying elements, as shown in Table 3-5. Generally, certain metals used as alloying elements for carbon steels such as nickel, chromium, etc., have pronounced effects in increasing the resistance to corrosion. Nickel improves corrosion resistance in steel by stabilizing the structure of the protective layer [92-95]. Chromium partially substitutes for iron ions in iron oxyhydroxide, which favourably forms a protective rust layer [96, 97]. The effects of the above alloy elements can lead to better corrosion resistance of S355J2 than that of P460NL2. The rust layer grew in thickness with prolonged exposure time, and gradually became rougher. After one year of exposure, the outer rust layer easily flaked off, clearly showing an accumulation of the corrosion products, as illustrated in Figure

4-2 (c) and (f).

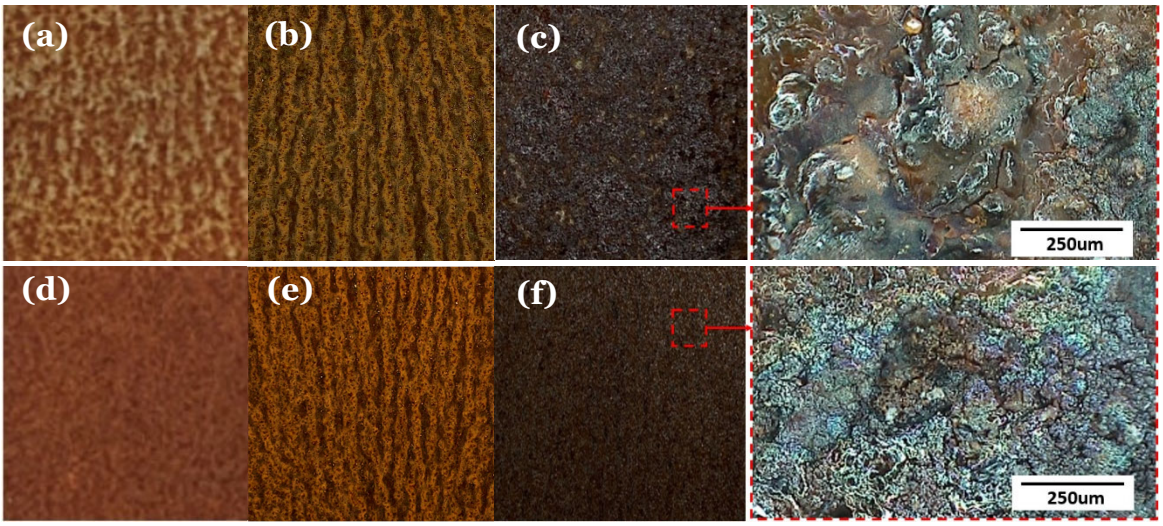

Figure 4-2. Morphology of rust layers on carbon steel in Knokke-Heist - S355J2 (top): (a) 1 month, (b) 3 months, (c) 12 months; P460NL2 (bottom): (d) 1 month, (e) 3 months, (f) 12 months.

Dissimilar welded T-joints displayed varying corrosion behaviours on the surfaces of typical zones in the initial stage of atmospheric corrosion, as depicted in Figure 4-3 to Figure 4-6. The rust formation initially appeared in the HAZ of carbon steel, and then rust layer formed in both the HAZ and BM of carbon steel (Figure 4-3). It is interesting to mention that no corrosion was observed on the duplex stainless steel surface, as well as across the weld metal and at the edges of the T-joint samples (see Figure 4-7). In addition to uniform corrosion, galvanic corrosion was visibly evident on the surface of carbon steel in contact with duplex EN1.4062 following a 12-month exposure, located in Knokke-Heist (Figure 4-6). An earlier investigation has concluded that duplex EN1.4062 is characterised by nobler corrosion potential compared to carbon steel S355J2 and P460NL2. Potential difference (+0.41 V) between studied lean duplex grade and carbon steel led to galvanic interactions, which can result in severe corrosion of carbon steel under the right atmospheric conditions, as discussed in Section 2.3.2.

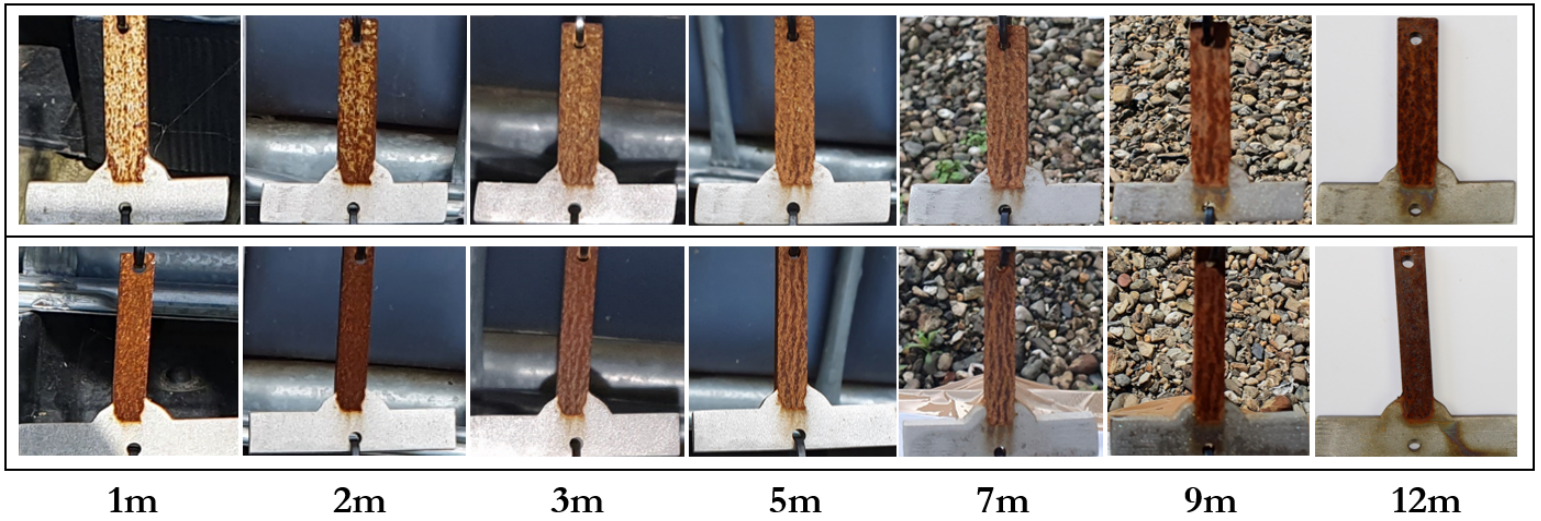

Figure 4-3. Aspect of the T-joint surface in Sint-Katelijne-Waver during exposure: S355J2 T-joint (top); P460NL2 T-joint (bottom).

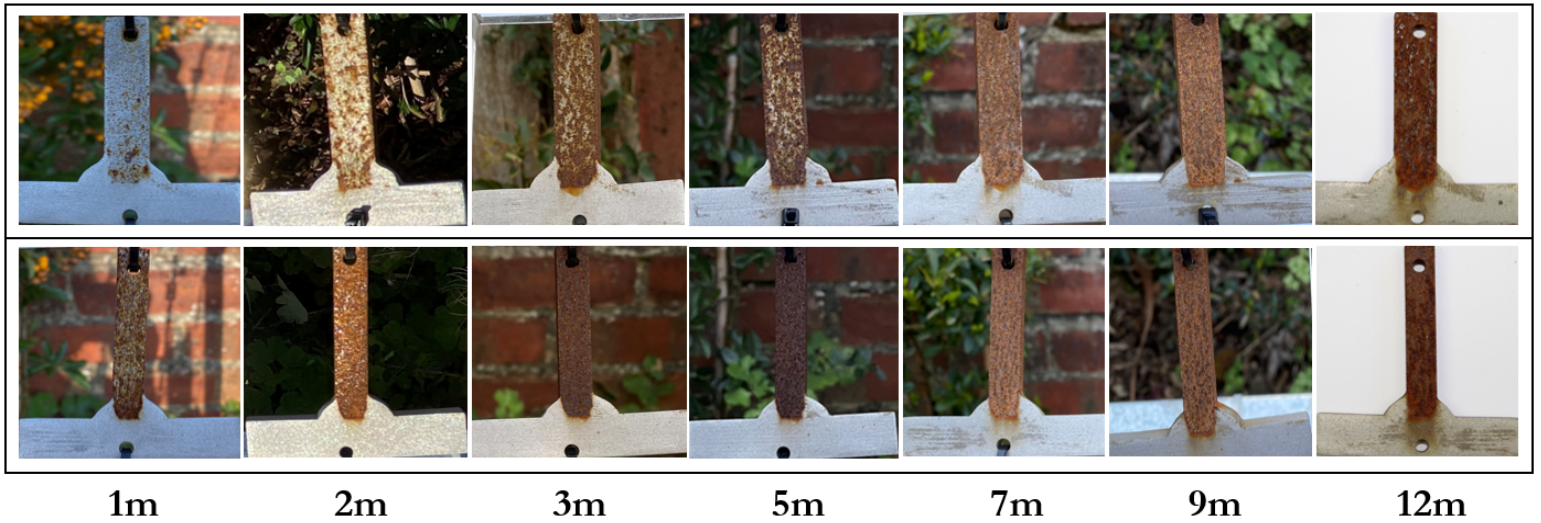

Figure 4-4. Aspect of the T-joint surface in Oxford during exposure: S355J2 T-joint (top); P460NL2 T-joint (bottom).

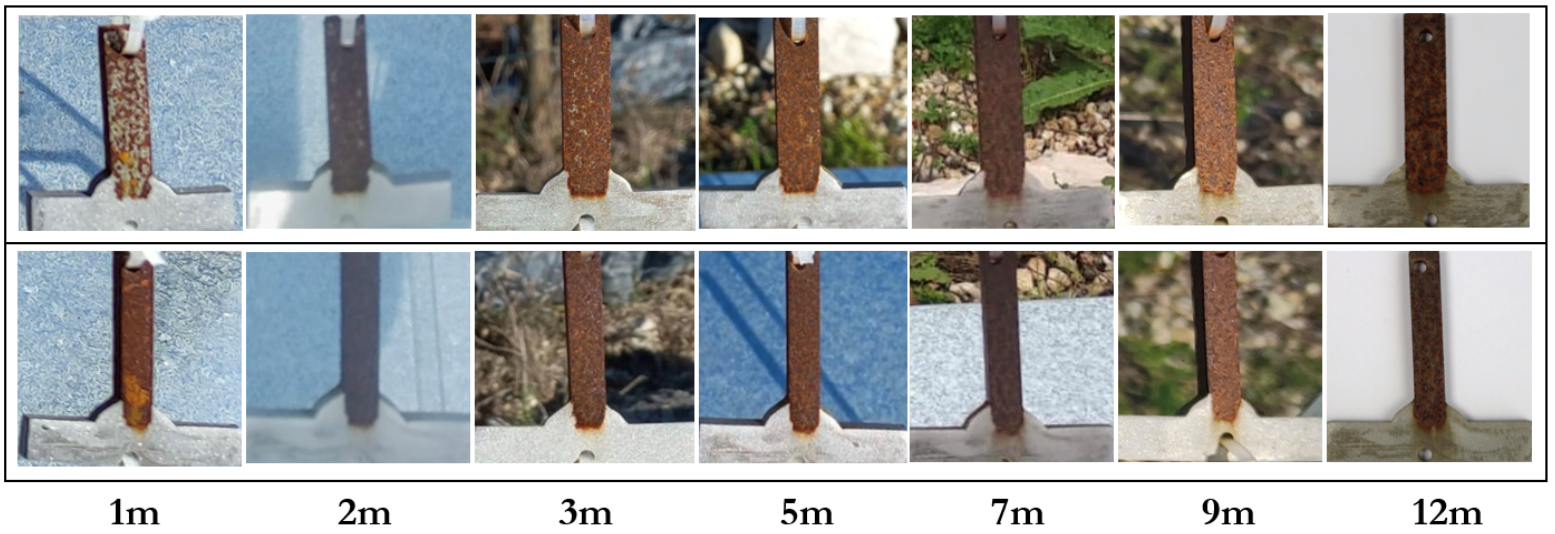

Figure 4-5. Aspect of the T-joint surface in Casalinho da Foz during exposure: S355J2 T-joint (top); P460NL2 T-joint (bottom).

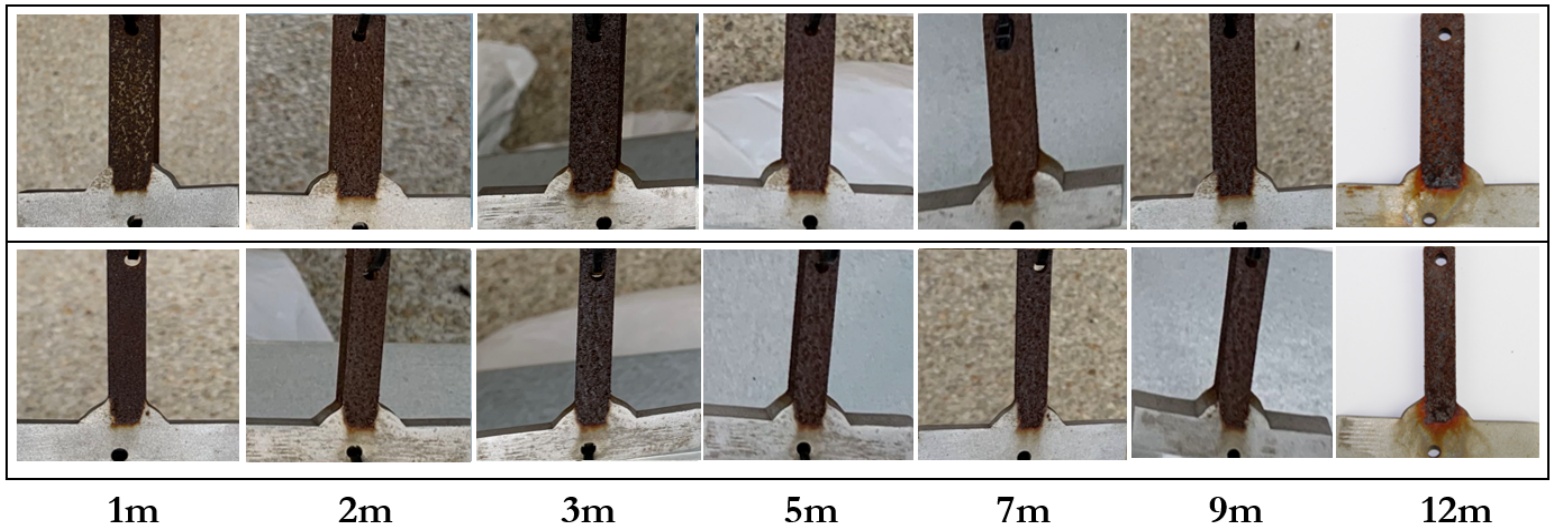

Figure 4-6. Aspect of the T-joint surface in Knokke-Heist during the exposure time: S355J2 T-joint (top); P460NL2 T-joint (bottom).

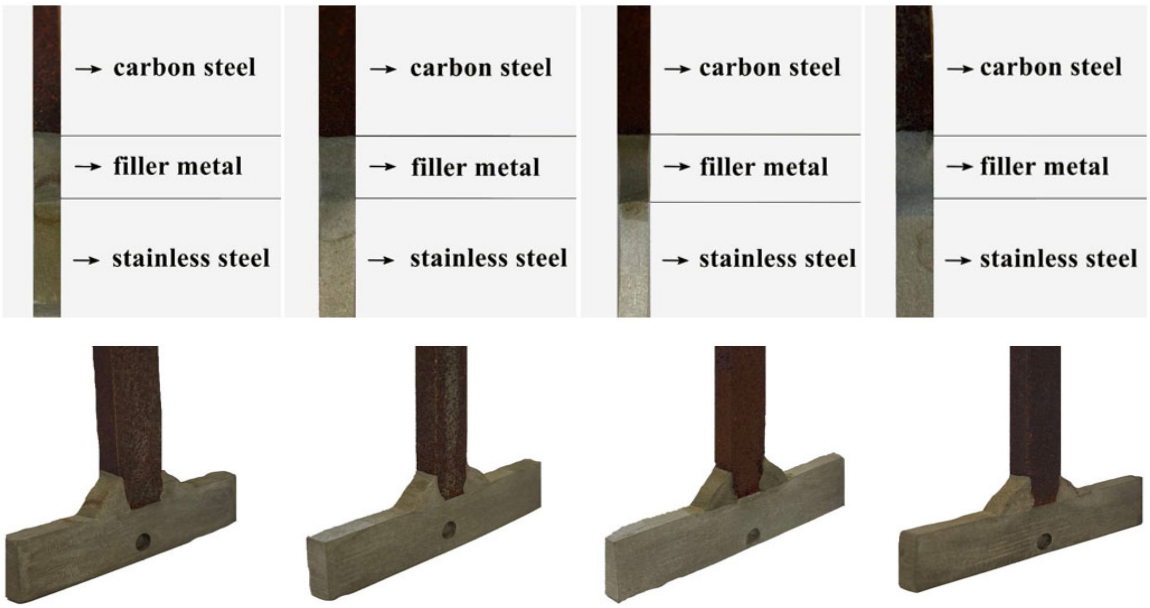

(a) (b) (c) (d)

Figure 4-7. Aspect on the edges of the samples after exposure: (a) Sint-Katelijne-Waver; (b) Oxford; (c) Casalinho da Foz; (d) Knokke-Heist.

Another interesting point to note is that the surface was covered by greyish-green rust layers in Knokke-Heist under the digital microscope, while yellow rusts also appeared on the metal surface in Sint-Katelijne-Waver, Oxford and Casalinho da Foz, as shown in Figure 4-8. The difference in the morphology of rusts can be attributed to the effect of rain wash. Based on the corrosion mechanisms of carbon steel, two rust layers form on the surface of carbon steel. The inner rust layer is characterised by a fine and compact structure, where the corrosion products mainly consist of *α-FeOOH* and Fe_3O_4 [97]. This layer can effectively restrain the penetration of rainwater. In contrast, the outer rust layer has a loose and porous nature, primarily due to the existence of *γ-FeOOH* [96, 97]. This layer is not stable, and the effect of rain wash may prevent part of outer rust layer from remaining on the surface. During the exposure period, Knokke-Heist had the least rainfall, as shown in Figure 4-1 (e).

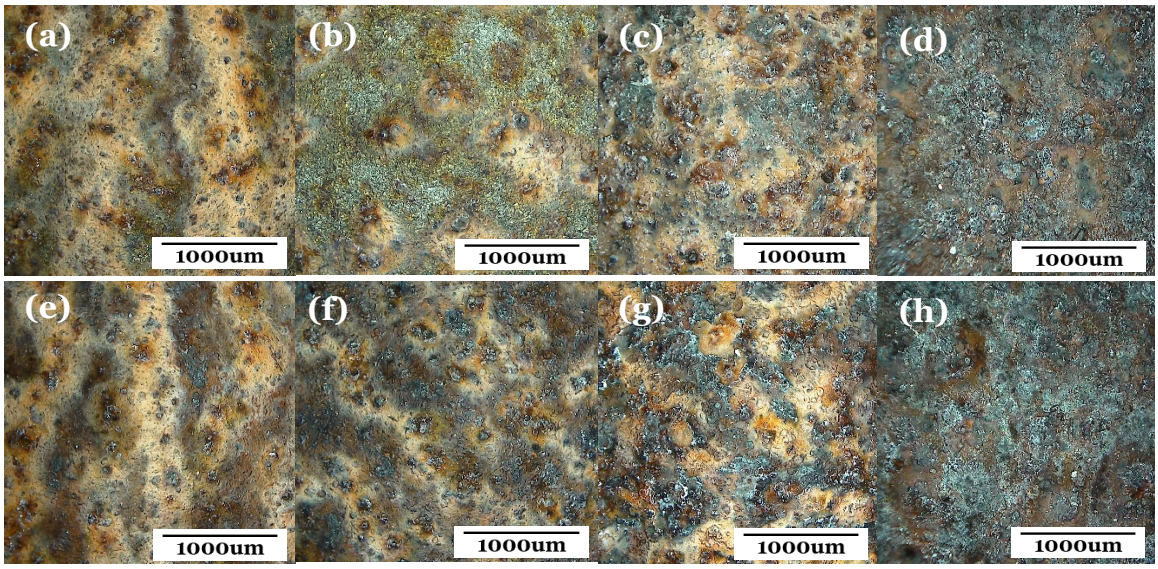

Figure 4-8. Macro-morphology of rust layers formed on carbon steel after 12 months S355J2 (top): (a) Sint-Katelijne-Waver; (b) Oxford; (c) Casalinho da Foz; (d) Knokke-Heist; P460NL2 (bottom): (e) Sint-Katelijne-Waver; (f) Oxford; (g) Casalinho da Foz; (h) Knokke-Heist.

4.3 Corrosion rates determined by weight loss

4.3.1 Overall mass loss

The corroded specimens were chemically cleaned (1000 mL solution with 100 mL of nitric acid and 20 mL of hydrofluoric acid; 25°C; 10 minutes) for six times until the mass loss stabilized. The mass loss shall be plotted as a function of the number of cleaning cycles, as shown in Figure 4-9 [88]. Point A signifies the mass loss of corroded specimens prior to the initiation of the cleaning process. In the majority of cases, two straight lines (AB and BC) can be observed: line AB represents the removal of corrosion products, while line BC depicts the removal of the steel substrate once the corrosion products have been eliminated [88]. Point D represents the mass of the steel substrate at zero cleaning cycles and can be obtained by extrapolating line BC to the ordinate axis [88]. The mass loss due to

corrosion will correspond approximately to point D. According to ASTM G1-90 [88], the corrosion rate (R_{corr}) can be extrapolated based on Equation 4-1.

$$R_{corr} = (K \times W)/(A \times t \times \rho) \quad 4\text{-}1$$

where R_{corr} is the corrosion rate, expressed in micrometres per year [µm/a], K is 8.76 x 10^7 (conversion factor), t is the time of exposure [h], A is the exposure area [cm^2], W is the mass loss [g], and ρ is the density of steel [g/cm^3].

One can see that, considering the effect of cleaning, the corrosion rates of lean duplex EN1.4062 were nearly negligible in Table 4-4, with values below 0.5 µm/a. However, carbon steels corroded significantly faster, as expected, due to the lack of a protective layer. It was visible that S355J2 base plates corroded less than P460NL2 which is now confirmed by the corrosion rate measurements[4]. ISO 9223 [89] defines the corrosivity categories, ranging from C1 to C5, and provides guiding values of the first-year corrosion rates for carbon steel for each corrosivity category (Table 4-3). The values of carbon steel (S355J2 and P460NL2) corrosion rate were below 25 µm/a, which were in the C2 corrosivity category. The corrosion rates of the T-shaped dissimilar joints were lower than those of the base plates. This is explained because of the presence of the austenitic stainless steel filler alongside the lean duplex grade forming the T-joint. In Table 4-4, the samples denoted N-S355J2 and N-P460NL2 represent the dissimilar welds of EN1.4062/ 309LSi, i.e., dissimilar T-joints in which the carbon steels S355J2 and P460NL2 were removed before exposure. No significant difference was measured between the corrosion rates of these samples, i.e., dissimilar welds EN1.4062/309LSi at the test sites, with values not exceeding 2.5 µm/a, implying that the austenitic weld metal and the heat-affected zone of stainless steel do not affect the corrosion resistance significantly.

[4] The morphology of carbon steels (S355J2 and P460NL2) rust layer is shown in Section 4.2.

Table 4-3. Corrosion rates of carbon steel for the first year of exposure for all different corrosivity categories based on ISO 9223 [89].

ISO corrosivity category	Corrosion rates of carbon steel (R_{corr}) [µm/a]
C1	$R_{corr} \leq 1.3$
C2	$1.3 < R_{corr} \leq 25$
C3	$25 < R_{corr} \leq 50$
C4	$50 < R_{corr} \leq 80$
C5	$80 < R_{corr} \leq 200$

Table 4-4. Corrosion rates determined by weight loss after the first year of exposure for all different test sites.

Test site	Corrosion rate [µm/a]						
	EN1.4062	S355J2	P460NL2	T-S355J2	T-P460NL2	N-S355J2	N-P460NL2
SKW	0.42	9.23	12.50	4.63	4.96	1.50	1.59
Oxford	0.47	10.10	13.29	5.74	5.93	1.60	1.68
Casalinho da Foz	0.40	13.12	15.69	6.46	6.89	1.72	1.80
Knokke-Heist	0.41	16.02	18.28	8.42	8.87	2.22	2.30

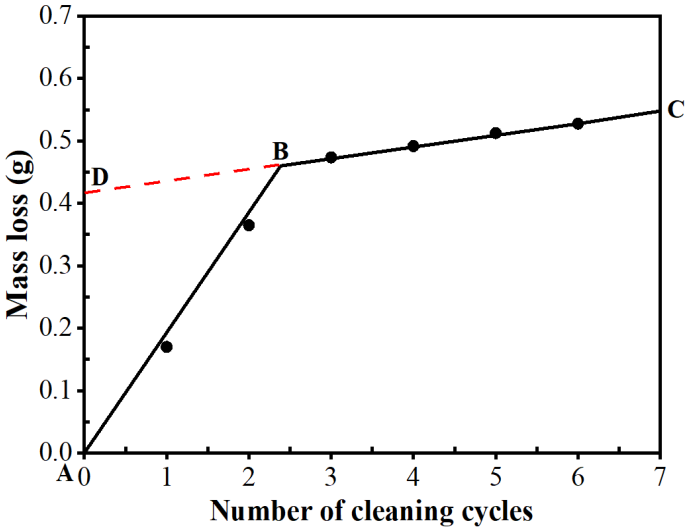

Figure 4-9. Stabilized mass loss after 6 repeated chemical cleaning (T-S355J2 in Knokke-Heist taken as an example).

4.3.2 Mass loss by decomposition

This study proposes to decompose a T-joint into its individual components, including EN1.4062 duplex, S355J2 or P460NL2 carbon steel, and 309LSi filler metal. Similarly, a carbon-removed joint can be broken down into EN1.4062 duplex and 309LSi filler metal. It is proposed to obtain the corrosion rates with respect to the individual components, which then becomes the decomposed corrosion rate, as schematically depicted in Figure 4-10. The corrosion rate of each individual component has been measured experimentally.

The decomposed corrosion rates of dissimilar welded T-joints are expected to match the measured corrosion rates theoretically. However, this comparison does not consider the potential effects such as dissimilar welding and galvanic corrosion. On the one hand, if the decomposed corrosion rates are equal to the measured rates, it suggests that dissimilar welded T-joints are not affected by dissimilar welding or galvanic corrosion; on the other hand, if the decomposed corrosion rates are smaller than the measured rates, it indicates that the effects of dissimilar welding and galvanic corrosion should not be disregarded. A comparison between the measured corrosion rates obtained through weight-loss measurements and the decomposed corrosion rates are displayed in Table 4-5. It is noteworthy that the measured corrosion rates of dissimilar welded T-joints are higher than the decomposed rates. This suggests that dissimilar welding, together with galvanic corrosion, has a noticeable impact on the corrosion behaviour, as can be seen in Section 2.3.

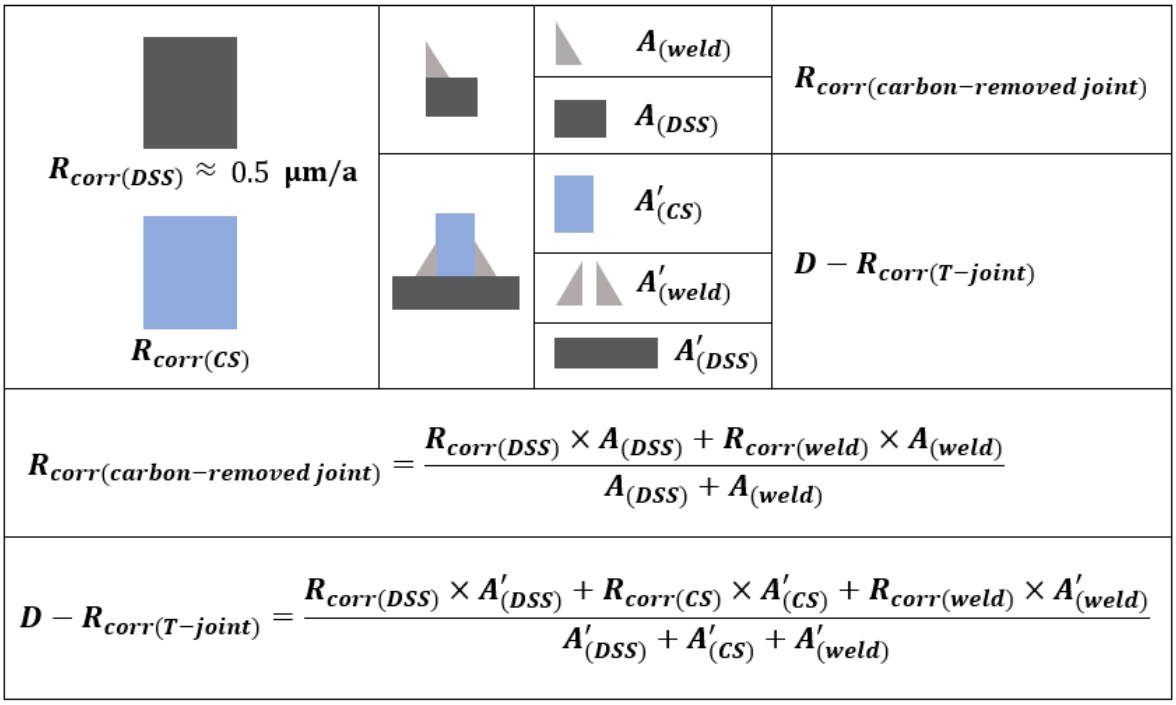

Where DSS is the duplex stainless steel, CS is the carbon steel, and $D\text{-}R_{corr}$ is the decomposed corrosion rate [µm/a].

Figure 4-10. Schematic of decomposed corrosion rate for dissimilar welded T-joints.

Table 4-5. Comparison of the measured and decomposed corrosion rates at the 4 test sites.

Test site	Corrosion rate [µm/a]				
	Measured: Base plate			Measured: Carbon-removed joint	
	EN1.4062	S355J2	P460NL2	S355J2-removed	P460NL2-removed
SKW	0.42	9.23	12.50	1.50	1.59
Oxford	0.47	10.10	13.29	1.60	1.68
Casalinho da Foz	0.40	13.12	15.69	1.72	1.80
Knokke-Heist	0.41	16.02	18.28	2.22	2.30

(continued)

Test site	Corrosion rate [µm/a]			
	T-S355J2		T-P460NL2	
	Measured by weight loss	Decomposed	Measured by weight loss	Decomposed
SKW	4.63	4.24	4.96	4.73
Oxford	5.74	5.27	5.93	5.59
Casalinho da Foz	6.46	5.92	6.89	6.47
Knokke-Heist	8.42	7.28	8.87	7.67

4.4 Localized corrosion evaluation

Localized corrosion analysis is essential since corrosion pits are typically the initial crack sites on the metal surface, which, for example under fatigue loading, can lead to crack propagation and structural failure even at applied stresses significantly lower than material's yield strength [98]. After undergoing a cleaning procedure, numerous corrosion pits were observed on the carbon steel base plates, as shown in Figure 4-11, as well as in the HAZ of carbon steel, as shown in Figure 4-12. Although the number and size of pits are important, the pit depth is a crucial parameter when assessing material failure. To illustrate the method of measuring the depth of pits using the Hirox KH-8700 digital microscope, several typical cloud maps are provided in Figure 4-13. To determine the pit depth, at least 20 pits were randomly selected from various zones of the specimen.

More and deeper pits were observed on the carbon steel base plate of grade P460NL2 compared to S355J2. This observation was confirmed in the previous section by the overall mass loss of carbon steels and visual examination of the rust layer on the carbon steels, as depicted in Figure 4-11. Figure 4-14 provides an overview of the pit depths measured on the carbon steel surface at four test sites. The results of pit depth are consistent with the corrosion rates determined by weight loss. In addition, more severe localized corrosion was observed in the HAZ of carbon steel. This can be attributed to decarburization and grain growth due to element diffusion during welding [2]. Notably, the pits found in the HAZ of carbon steel were significantly deeper in Knokke-Heist, where the surface had deteriorated completely due to the high chloride deposition rate. This suggests that dissimilar welds exposed to salt-rich environments (such as close distance to the sea or presence of de-icing salt) should be protected by a coating system, particularly in the HAZ of carbon steel grade. Furthermore, the distinct contrast

in chromium and nickel content between EN1.4062 base metal and the 309LSi filler metal results in a clearly discernible fusion line, which is clearly visible when analysed using EDS. The SEM provides the highest possible magnification, enabling the observation of pits in detail. However, no pits were detected in the HAZ between the austenitic 309LSi filler and EN1.4062 lean duplex at any test locations, as shown in Figure 4-15, which is expected due to the protective films formed on both grades.

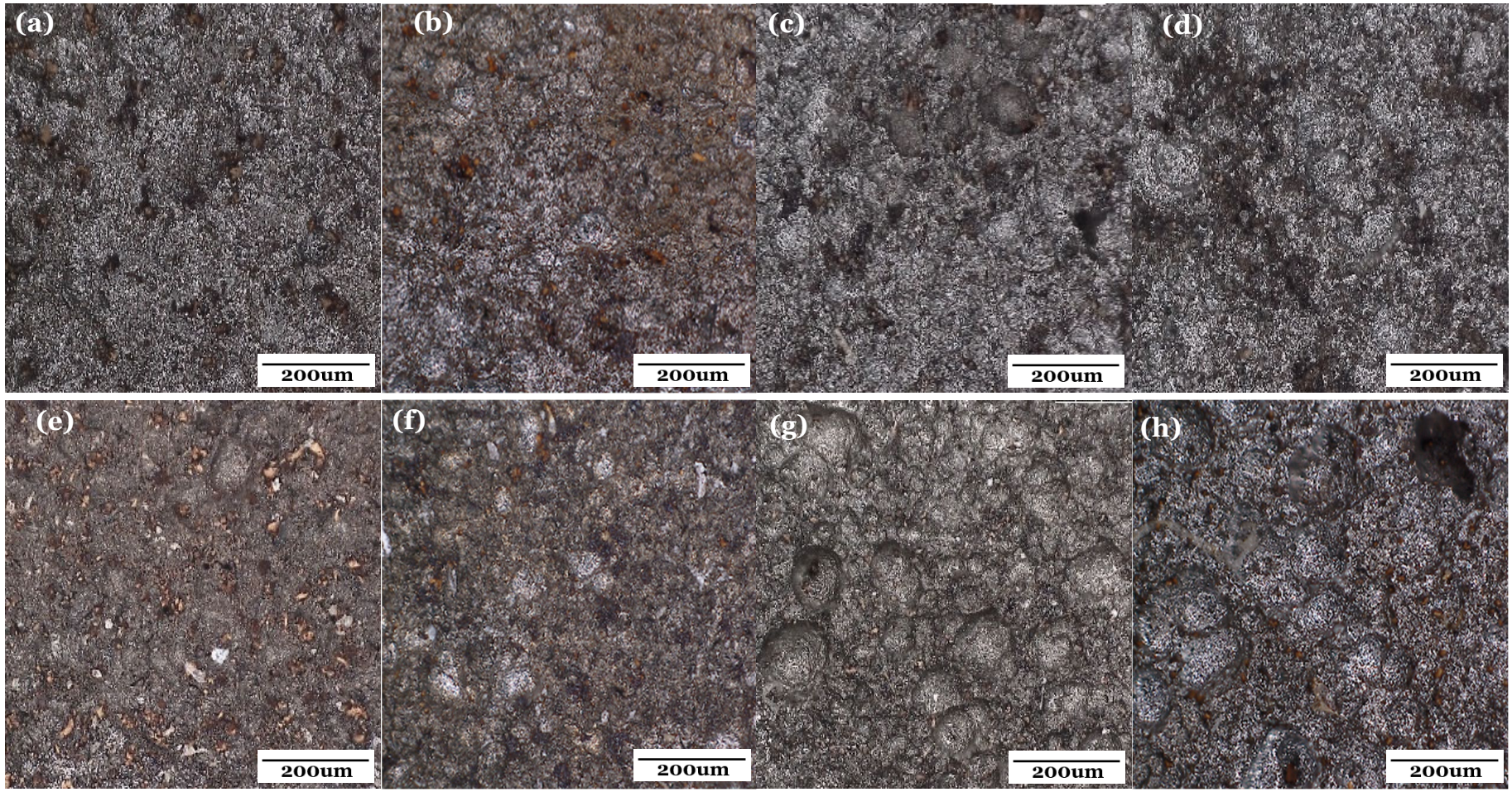

Figure 4-11. Pits on the carbon steel base plate after the cleaning procedure - S355J2 (top): (a) Sint-Katelijne-Waver; (b) Oxford; (c) Casalinho da Foz; (d) Knokke-Heist; P460NL2 (bottom): (e) Sint-Katelijne-Waver; (f) Oxford; (g) Casalinho da Foz; (h) Knokke-Heist.

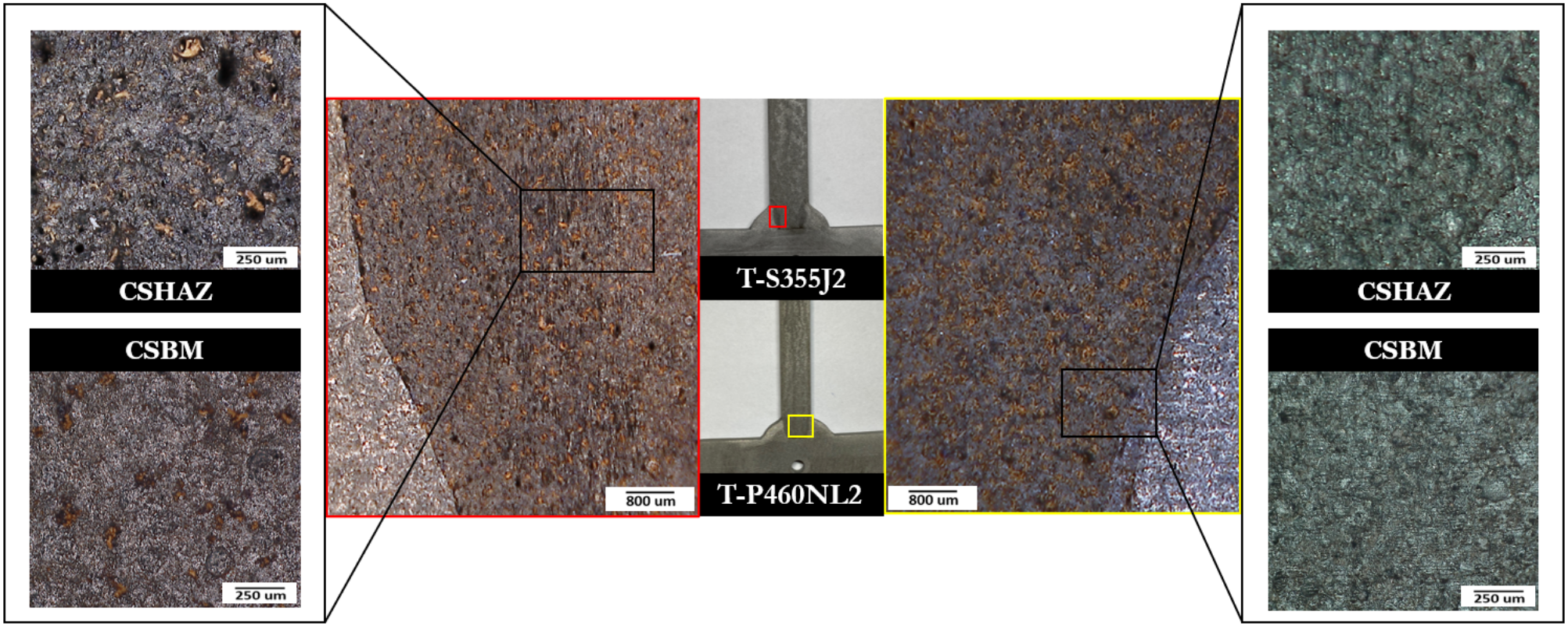
250 um
CSHAZ
CSBM
250 um
800 um
T-S355J2
T-P460NL2
800 um
250 um
CSHAZ
CSBM
250 um

(a)

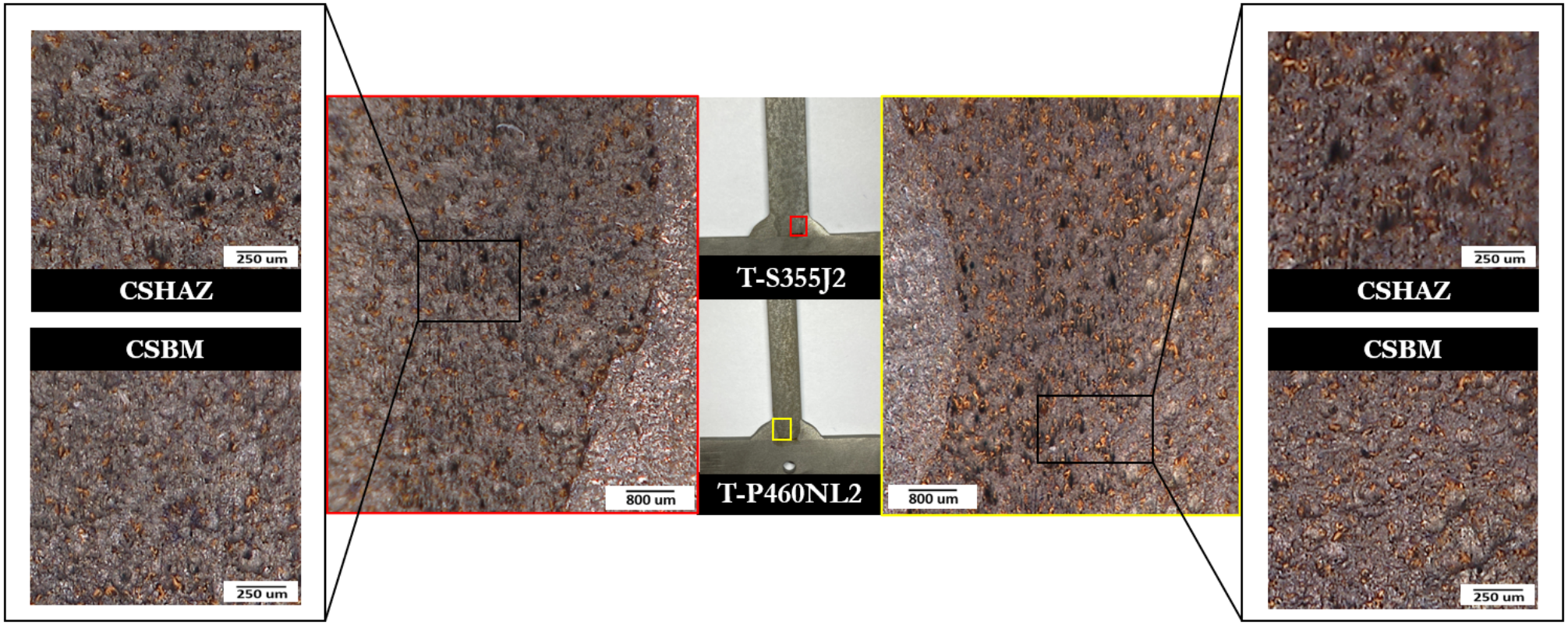
CSHAZ
250 um
CSBM
250 um
800 um
T-S355J2
T-P460NL2
800 um
CSHAZ
250 um
CSBM
250 um

(b)

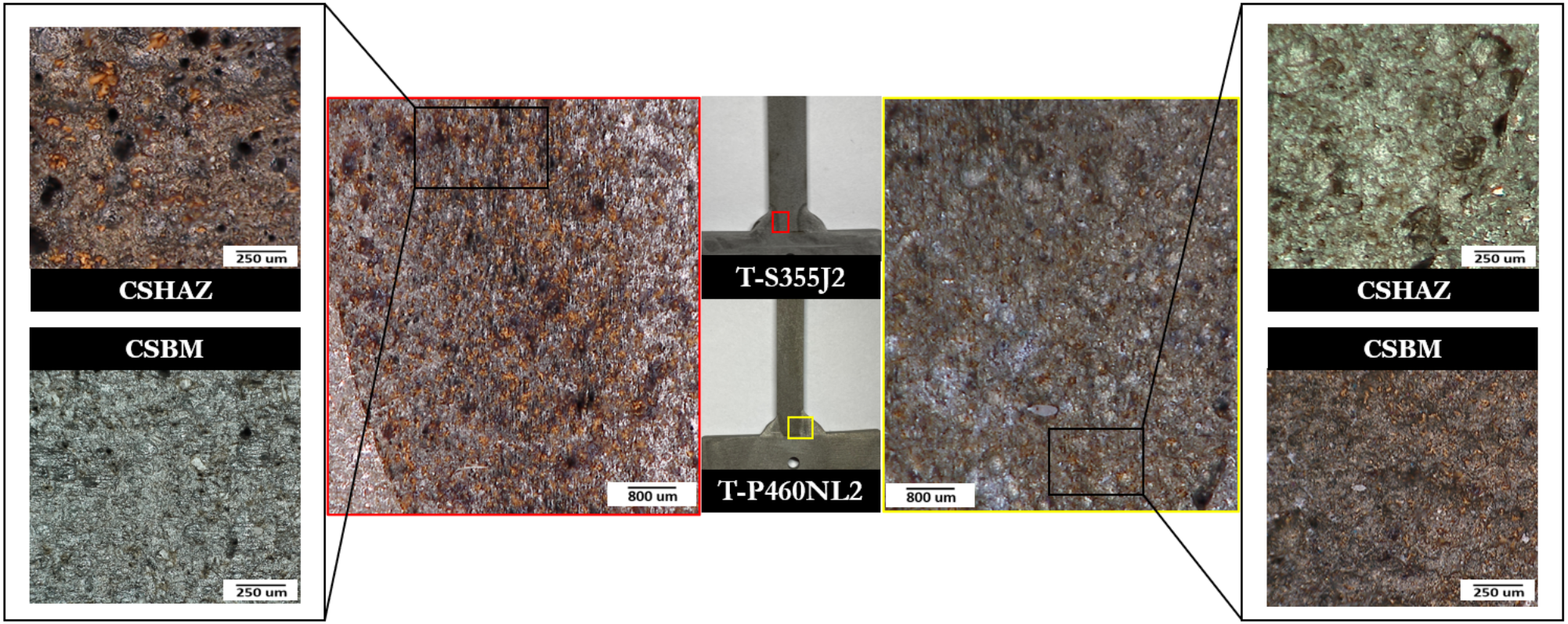
250 um
CSHAZ
CSBM
250 um
800 um
T-S355J2
T-P460NL2
800 um
250 um
CSHAZ
CSBM
250 um

(c)

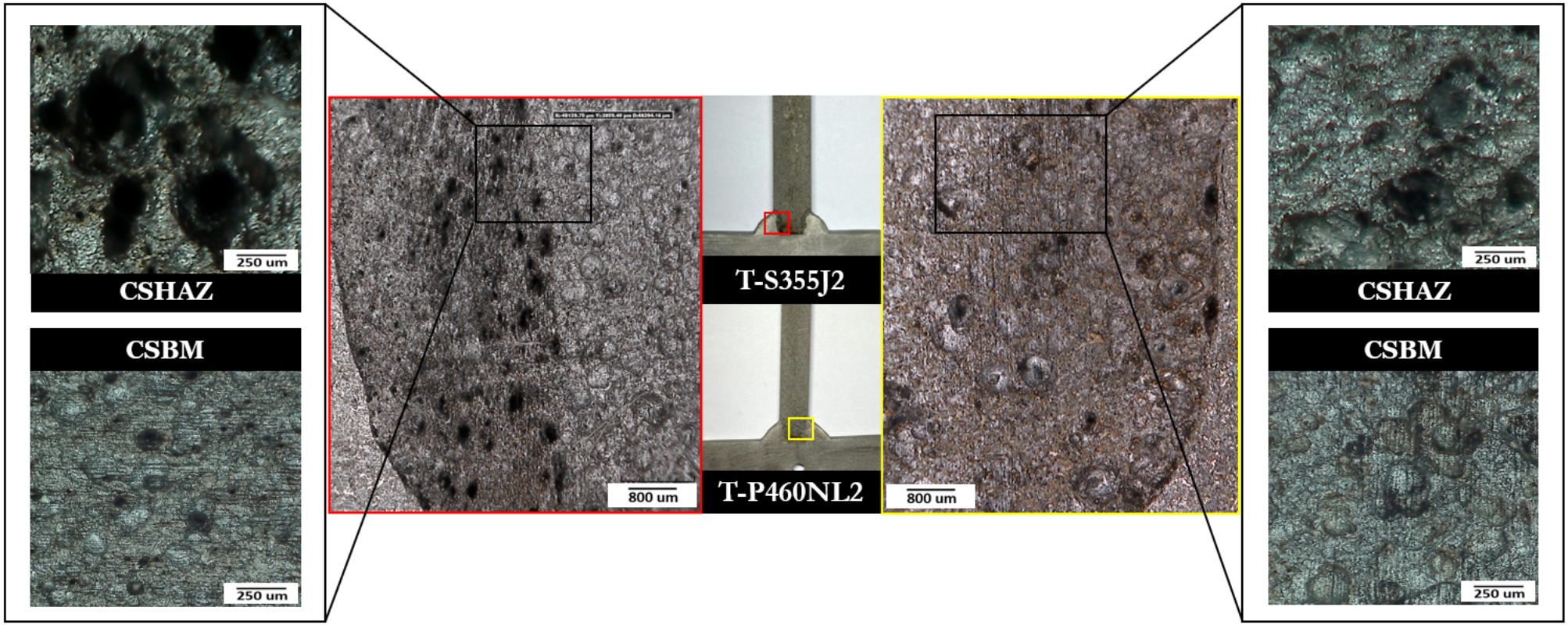

(d)

Figure 4-12. Pits on the HAZ and BM of carbon steel (S355J2 and P460NL2) after the cleaning procedure: (a) Sint-Katelijne-Waver; (b) Oxford; (c) Casalinho da Foz; (d) Knokke-Heist.

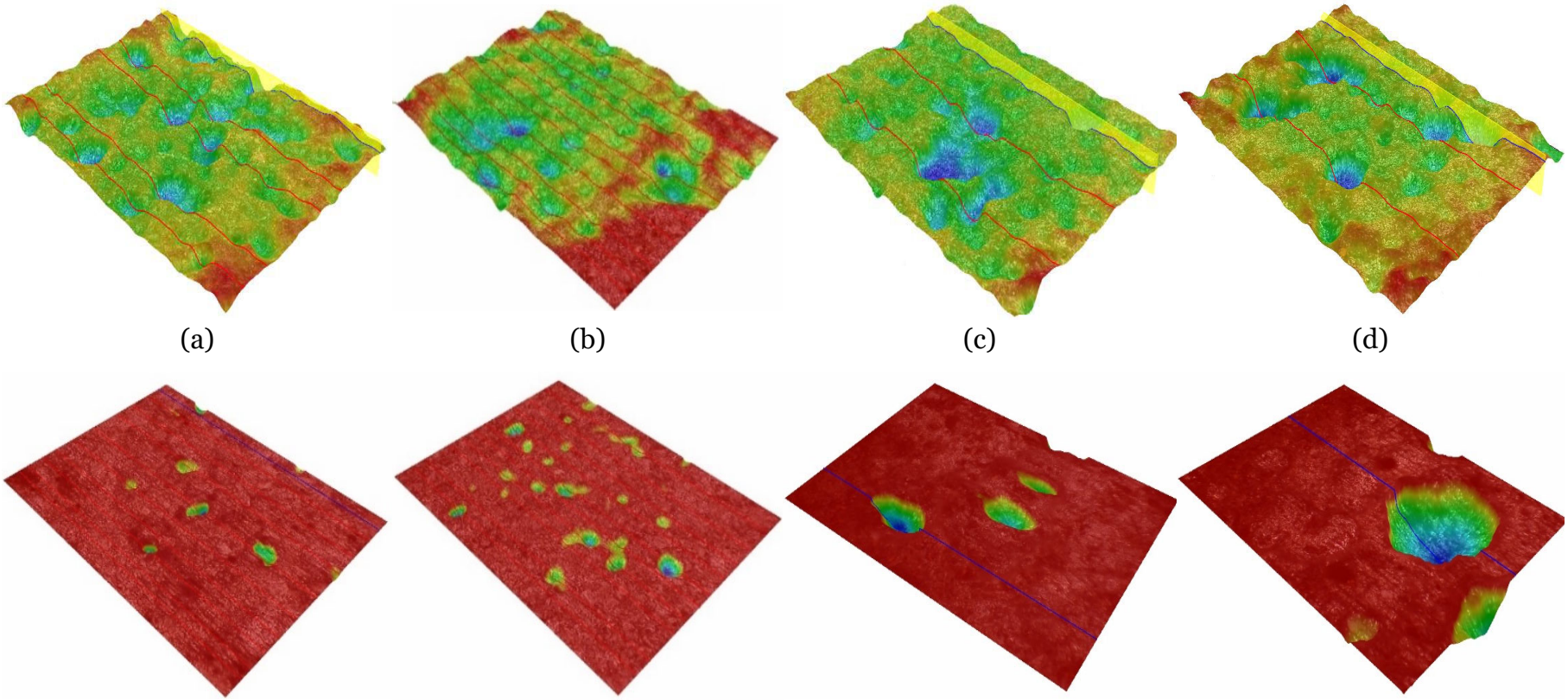

Figure 4-13. Typical mapping of pits depths and extent on carbon steel surface, magnification 100 μm. Carbon steel base metal: (a) Sint-Katelijne-Waver; (b) Oxford; (c) Casalinho da Foz; (d) Knokke-Heist; The carbon steel heat-affected zone: (e) Sint-Katelijne-Waver; (f) Oxford; (g) Casalinho da Foz; (h) Knokke-Heist.

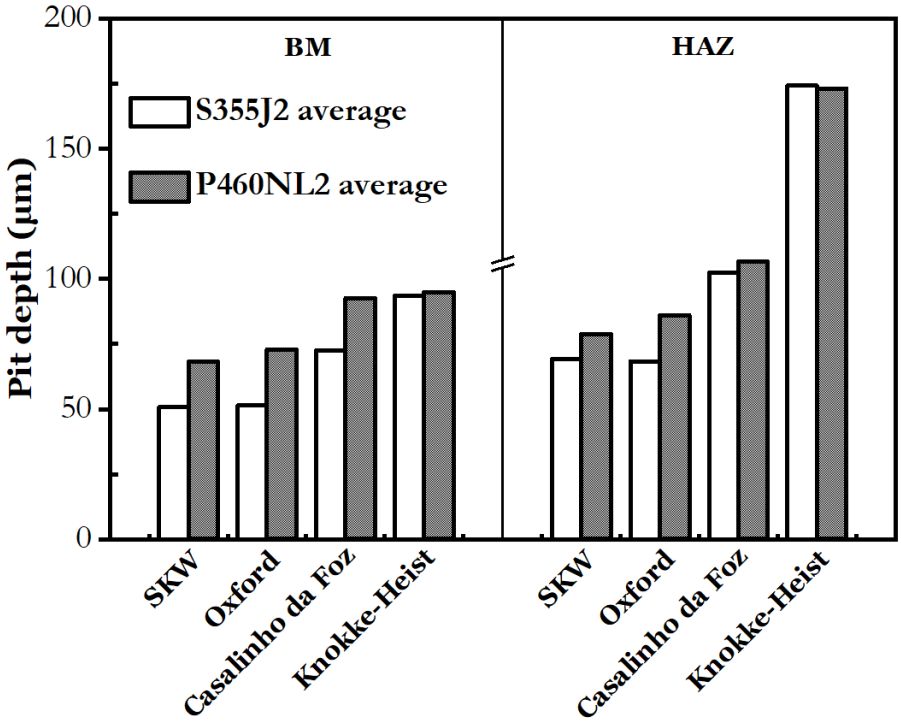

Figure 4-14. Average pit depth on the surface of carbon steels.

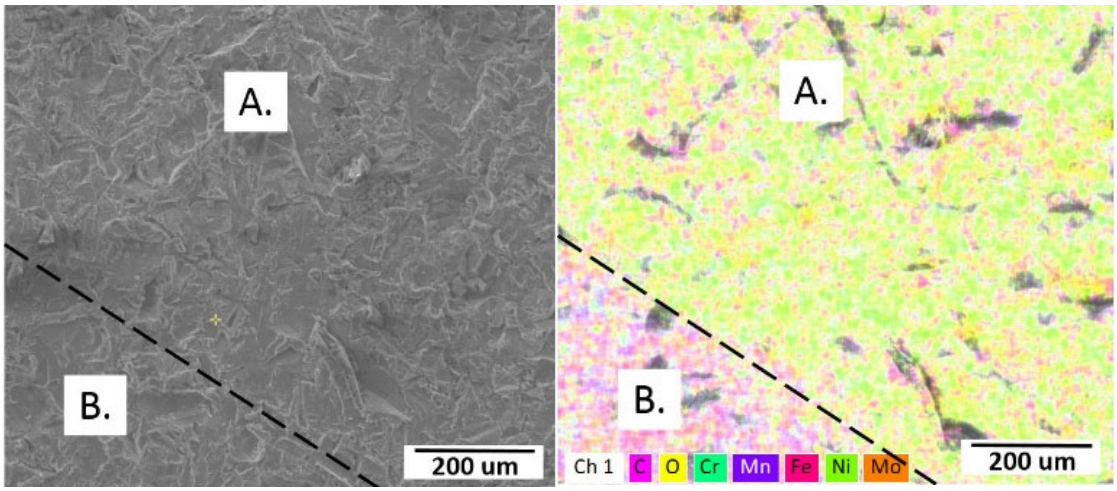

Figure 4-15. EDS analysis of dissimilar T-joint between EN1.4062 (A) and 309LSi (B) after exposure, where the fusion line is highlighted and no pitting visible in the HAZ.

5

Corrosion Evaluation

5.1 Estimated corrosion rate

The guidance ISO 9223 [89] provides a dose-response function (Equation 5-1) to estimate the first-year atmospheric corrosion loss of carbon steel based on environmental factors. The dose-response function is a relationship obtained from exposure tests results. It considers annual average values of environmental parameters. The environmental factors described in Chapter 4 (relative humidity, temperature, time of wetness, sulphur dioxide deposition rate, and chloride deposition rate) which play key roles in atmospheric corrosion, are utilized to predict the atmospheric corrosion of carbon steel. The input environmental variables in this study are presented in Table 4-2.

$$R_{corr} = 1.77 \times P_d^{0.52} \times e^{0.020 \times RH + f(T)} + 0.102 \times S_d^{0.62} \times e^{0.033 \times RH + 0.040 \times T} \qquad 5\text{-}1$$

$$f(T) = 0.150 \times (T - 10) \quad T \leq 10\ ℃$$

$$f(T) = \text{-}0.054 \times (T - 10) \quad T > 10\ ℃$$

where R_{corr} is the predicted first-year corrosion rate of carbon steel [μm/a], T is the annual average temperature [°C], RH is the annual average relative humidity [%], P_d is the annual average sulphur dioxide deposition rate [mg/(m²·d)], S_d is the

annual average chloride deposition rate [mg/(m²·d)] and $f(T)$ is a correction factor, specifically for steel. Several dose-response functions have been developed in the literature with the aim to estimate the annual corrosion rate of carbon steel in specific atmosphere, using the aforementioned key environmental factors as independent variables. Table 5-1 presents a compilation of these published dose-response functions.

Table 5-1. Dose-response functions for carbon steel corrosion published in the literature.

Function	N	Variable	Ref. (year)
Lien & San			
$R_{corr} = 0.0157 \times RH^{2.3} \times \left(\frac{\tau}{3800}\right)^{0.15} \times \left(1+\frac{P_d}{50}\right)^{0.22} \times e^{-0.0019\times(T+20)}$	21	RH, T, P_d, τ	[99] (2002)
Knotkova et al.			
$R_{corr} = 0.091 \times P_d^{0.56} \times \tau^{0.52} \times e^{f(T)} + 0.158 \times S_d^{0.58} \times \tau^{0.25} \times e^{0.05\times T}$ $f(T) = 0.103\times(T-10) \quad T \le 10°C$ $f(T) = -0.059\times(T-10) \quad T > 10°C$	125	T, P_d, S_d, τ	[100] (2003)
Klinesmith et al.			
$R_{corr} = 13.4 \times \left(\frac{\tau}{3800}\right)^{0.46} \times \left(1+\frac{P_d}{25}\right)^{0.62} \times \left(1+\frac{S_d}{50}\right)^{0.34} \times e^{0.02\times(T+20)}$	190	T, P_d, S_d, τ	[101] (2007)
Knotkova et al.			
$R_{corr} = 0.09 \times S_d^{0.56} \times \tau^{0.53} \times e^{f(T)} + 0.24 \times P_d^{0.47} \times \tau^{0.25} \times e^{0.05\times T}$ $f(T) = 0.098\times(T-10) \quad T \le 10°C$ $f(T) = -0.087\times(T-10) \quad T > 10°C$	119	T, P_d, S_d, τ	[102] (2010)
Standard ISO 9223			
$R_{corr} = 1.77 \times P_d^{0.52} \times e^{0.02\times RH + f(T)} + 0.102 \times S_d^{0.62} \times e^{0.033\times RH + 0.04\times T}$ $f(T) = 0.150\times(T-10) \quad T \le 10°C$ $f(T) = -0.054\times(T-10) \quad T > 10°C$	128	RH, T, P_d, S_d	[89] (2012)

Where N: number of data points; R_{corr}: the first-year corrosion rate of carbon steel [μm/a]; T: the annual average temperature [°C]; RH: the annual average relative humidity [%]; τ: the annual average time of wetness [h/a]; P_d: the annual average sulphur dioxide deposition rate [mg/(m²·d)]; S_d: the annual average chloride deposition rate [mg/(m²·d)]; $f(T)$: a correction factor.

To evaluate the fitness of published dose-response functions to predict our results, a comparison has been conducted between the corrosion rates estimated using dose-response functions and the measured corrosion rates (Figure 5-1). Regarding carbon steel, it can be noted that the corrosion rates predicted by the standard ISO 9223 model [89], as well as the functions proposed by Knotkova et al. (2003) [100] and Knotkova et al. (2010) [102], all fall within the C2 corrosivity category, as presented in Table 5-2, and the predicted values exhibit a relatively close proximity to the corresponding measured corrosion rates. Consequently, these models can be regarded as effective in their performance. However, these three models tend to underestimate the corrosion loss in Casalinho da Foz while overestimating it in Oxford. This can be attributed to the relatively significant influence of sulphur dioxide deposition rate on the corrosion rate within these functions. In cases where the sulphur dioxide deposition rate is low (P0 level), it can hinder the impact of other environmental variables on the corrosion rate, thereby leading to inaccurate corrosion rate predictions. It is worth noting that the predicted values obtained from the dose-response functions proposed by Lien & San (2002) [99] and Klinesmith et al. (2007) [101] exhibit significant overestimations compared to the other functions. This can be attributed to the fact that these two functions are calibrated for marine environment, which is known to be more aggressive compared to other environments.

In conclusion, the coefficients of each dose-response function are derived from environmental data collected at specific test sites. Extrapolating these functions to environments with varying levels of weather parameters may result in a reduction in accuracy. Therefore, further evaluation is necessary to identify an appropriate function suitable for results from the test sites with similar climatic conditions to this study, hence characterised by sulphur dioxide deposition rate (P0 level), chloride deposition rate (S1 level), and time of wetness (τ4 level).

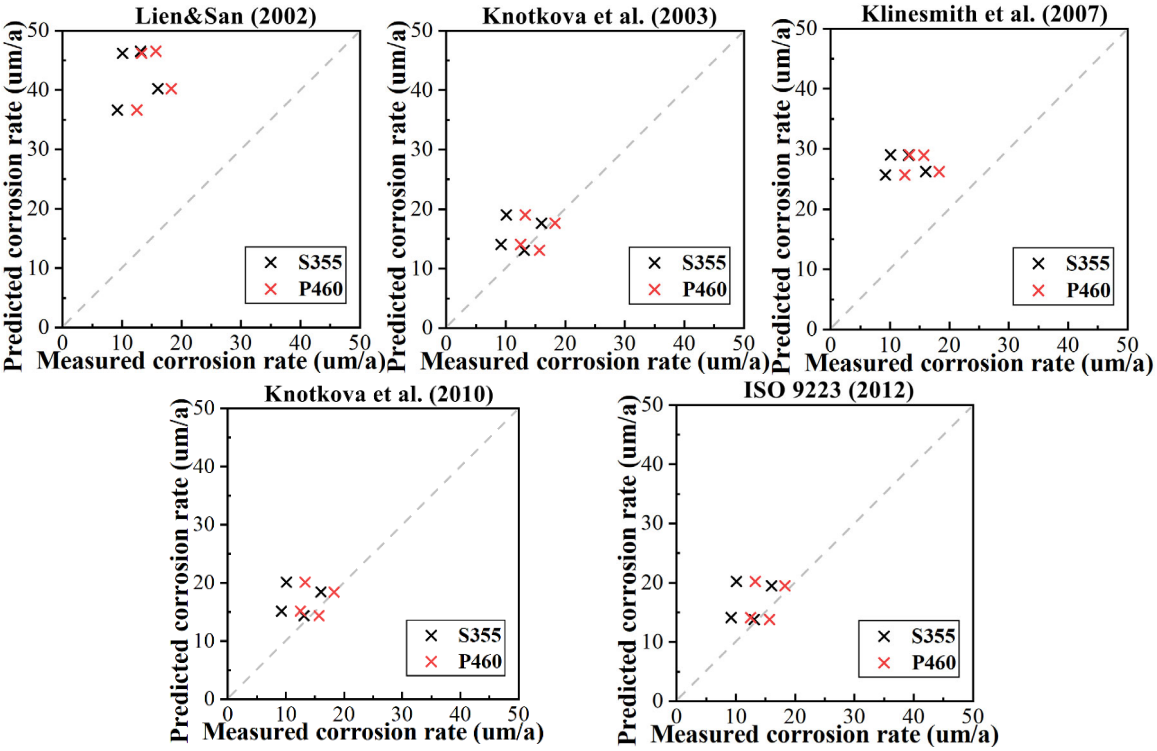

Figure 5-1. Comparison between the corrosion rates estimated using dose-response functions and the measured corrosion rates.

Table 5-2. Comparison between the estimated corrosion rates and the measured ones.

Test sites	Measured corrosion rate		Estimated corrosion rate				
	[g/(m²·a)]		[g/(m²·a)]				
	S355J2	P460NL2	[99]	[100]	[101]	[102]	[89]
Sint-Katelijne-Waver	9.23	12.50	36.64	14.05	25.67	15.14	14.12
	(C2)	(C2)	(C3)	(C2)	(C3)	(C2)	(C2)
Oxford	10.10	13.29	46.19	19.03	29.02	20.13	20.21
	(C2)	(C2)	(C3)	(C2)	(C3)	(C2)	(C2)
Casalinho da Foz	13.12	15.69	46.52	13.08	28.98	14.36	13.79
	(C2)	(C2)	(C3)	(C2)	(C3)	(C2)	(C2)
Knokke-Heist	16.02	18.28	40.24	17.65	26.25	18.42	19.48
	(C2)	(C2)	(C3)	(C2)	(C3)	(C2)	(C2)

5.2 Dose-response function calibration

In this chapter, the main objective is to determine an optimized dose-response function for accurately estimating the first-year atmospheric corrosion of carbon

steels. To achieve this goal, a method utilizing Spearman correlation analysis is employed to screen and identify the key environmental variables. Additionally, corrosion data related to carbon steel grades exposed to atmospheric conditions similar to those examined in this study are gathered from scholarly literature sources. Following the data collection process, a careful manual selection is conducted to ensure the inclusion of relevant and reliable corrosion datasets. Subsequently, the acquired corrosion dataset is utilized to calibrate the coefficients of the environmental variables within the dose-response function. Finally, the selection of the optimized dose-response function, which exhibits the highest predictive capacity, is determined by considering a range of evaluation metrics.

5.2.1 Key environmental variable screening

The corrosion is influenced by multiple environmental factors simultaneously. Prior to identifying an appropriate function of the first-year carbon steel corrosion rate, it is crucial to perform preliminary analyses to unveil any relationships among the environmental variables. This study uses the Spearman correlation coefficient as the evaluation metric to carry out the correlation analysis among six environmental variables, i.e., temperature, rainfall, humidity, chloride, sulphur dioxide and time of wetness. The values of Spearman correlation coefficients are in the range from −1 to 1. A positive sign indicates that the two series exhibit the same variation trend, meaning they increase or decrease simultaneously; while a negative sign indicates that the variation trends of the two series are diametrically opposed [103]. The Spearman correlation coefficient value approaching 1 or -1 indicates a stronger tendency between the two variables [103].

Figure 5-2 illustrates the results of the Spearman correlation coefficients between each pair of environmental factors over the one-year exposure period. Figure 5-3 presents the correlation between each pair of environmental variables in the form

of scatter plots, offering a visual representation of any relationships. Rainfall and humidity both indicate the moisture content of the air; thus, they have a strong correlation, with values of 0.86. As temperature has a strong correlation with humidity (-0.72), it also possesses a high Spearman correlation coefficient value with rainfall (-0.67). Looking at the other two environmental variables, chloride has medium correlation with temperature (-0.53), while sulphur dioxide has little to no correlation with other factors, with most values below 0.2. It should be noted that the correlation coefficient between time of wetness and humidity is 0.92, expectedly indicating an extremely high correlation between these two variables [104, 105]. Although rainfall shows high Spearman correlation coefficients with humidity and temperature, it is usually considered less important than the other two parameters in the literature. Considering this, the key factors selected to analyse the effect on atmospheric corrosion should be the temperature, humidity (or time of wetness), chloride, and sulphur dioxide.

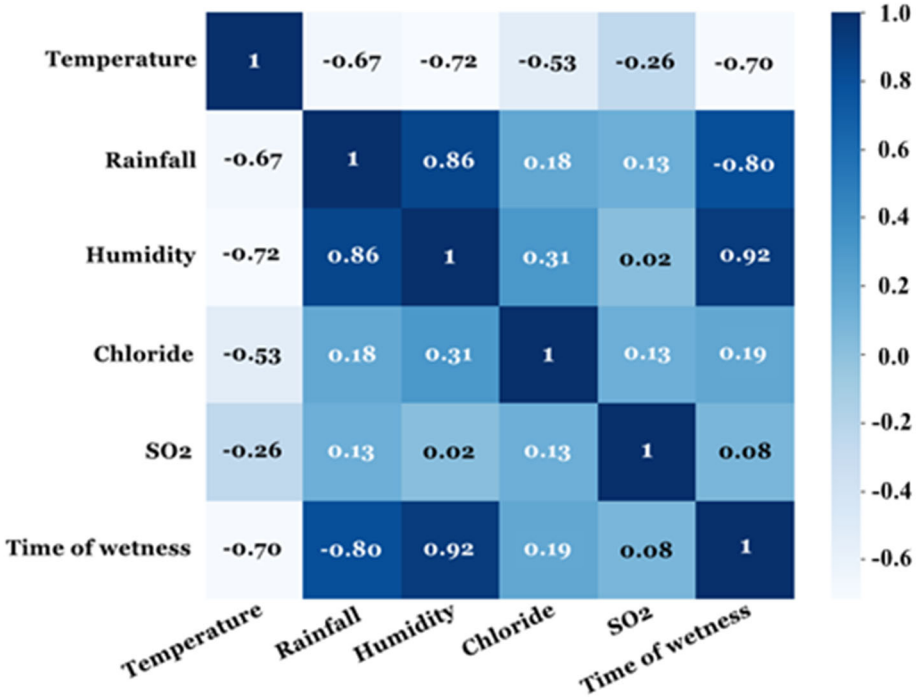

Figure 5-2. Spearman correlation coefficients between environmental factors.

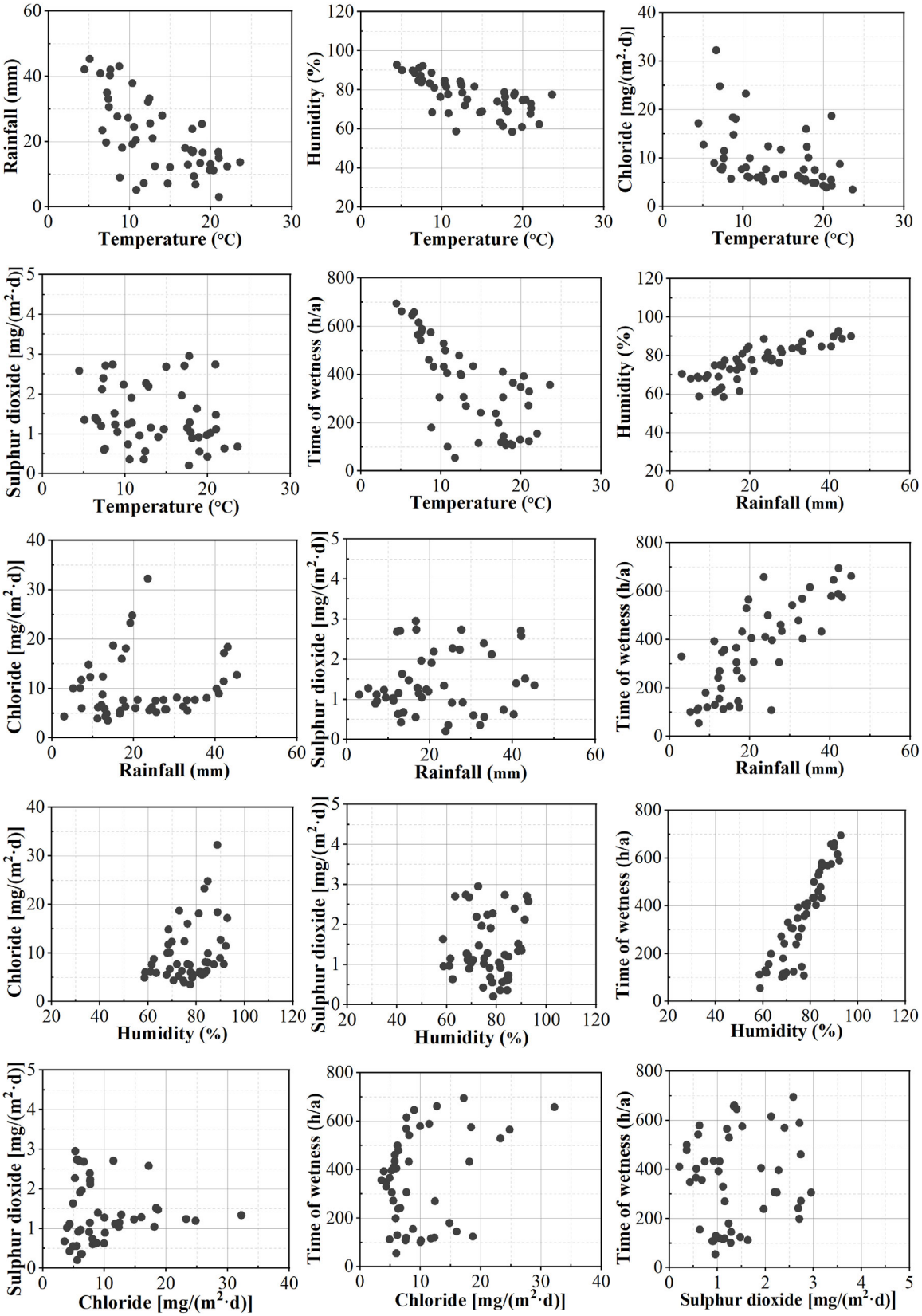

Figure 5-3. Correlation between each pair of environmental factors.

5.2.2 Corrosion database

Our study incorporates 2 grades of carbon steel (S355J2 and P460NL2) and 4 environmental conditions (Sint-Katelijne-Waver, Oxford, Casalinho da Foz, and Knokke-Heist). For each carbon steel grade, three sets of measurement data were obtained for each test site, resulting in a total of 24 corrosion data points.

In addition to this set of results, pertinent information from the literature was gathered. Specifically, corrosion data pertaining to carbon steel grades exposed to atmospheric corrosion similar to those examined in this study were collated. The collated data brings together multiple databases from a range of study programmes, e.g., ISOCORRAG [102], MICAT [106], and ICP/UNECE [106]. The reference reports and papers are presented in Table 5-3, indicating which environmental parameters were measured and reported by the authors. It is noteworthy that the time of wetness data has not been considered in some programmes [106-110]. However, Figure 5-3 illustrates the linear relationship between the time of wetness and the relative humidity, enabling the estimation of the corresponding time of wetness values based on relative humidity.

Prior to statistically analysing the data collected from the literature, manual data filtering process has been carried out, based on the following criteria:

1. The corrosivity category must be C2, i.e., characterised by little or no degree of atmospheric pollution [89].
2. The time of wetness must be maintained at a level below 5500 h/a, while the sulphur dioxide deposition rate and chloride deposition rate must be kept below 4 mg/(m^2·d) and 60 mg/(m^2·d) respectively.
3. In cases where meteorological or pollution data are missing from the reference, the data is removed from the database.

After manual selection, the screened database consists of 50 corrosion data points obtained from various locations worldwide (see Figure 5-4 and APPENDIX B).

Table 5-3. Reports and papers used in this study, sourced from the literature.

Database	N	T	RH	τ	P_d	S_d
ISOCORRAG [102]	51	×	×	×	×	×
MICAT [106]	75	×	×	×	×	×
ICP/UNECE [106]	39	×	×	○	×	×
Singh et al. [107]	4	×	×	○	×	×
Marco et al. [108]	2	×	×	○	×	×
Huang et al. [109]	6	×	×	○	×	×
Sica et al. [110]	15	×	×	○	×	×
Thandar et al. [111]	3	×	○	×	×	×
Seechurn et al. [112]	4	×	×	×	×	×
Prosek & Tidblad [113]	42	×	×	×	×	×
Coburn et al. [114]	46	×	×	×	×	×
Palsson et al. [115]	4	×	×	×	×	×

N: Number of data points.

× means data measured, available in the reference paper; ○ means data re-calculated by us.

(a) South America

(b) Europe

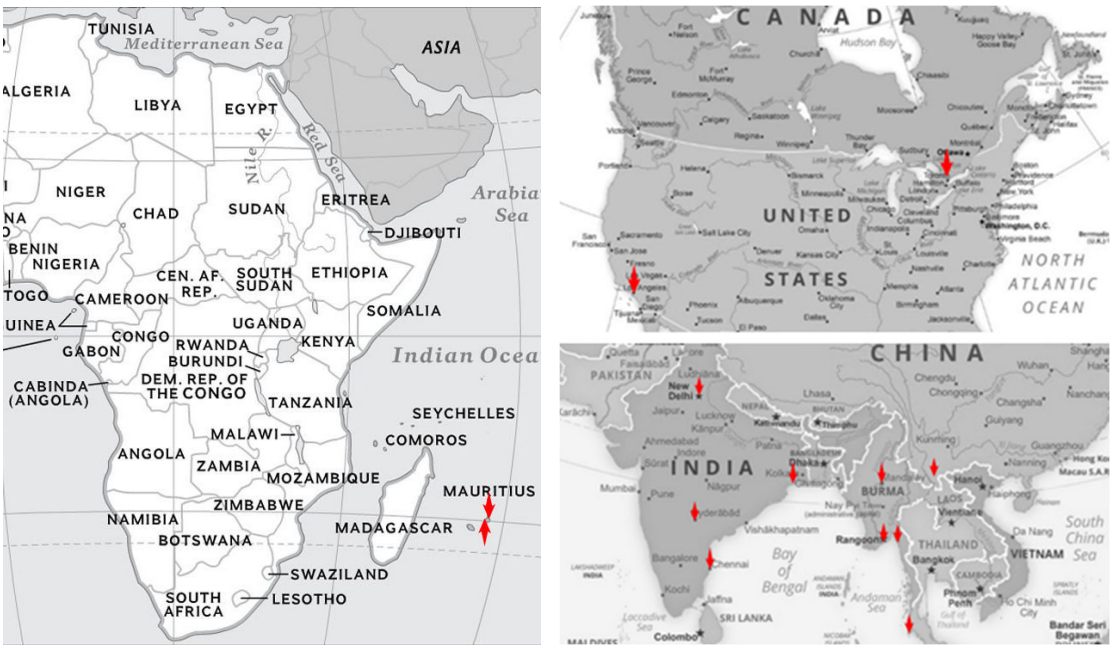

(c) Africa (d) Asia and North America

Figure 5-4. Maps of atmospheric corrosion test sites gathered in the literature.

5.2.3 Calibration of the model coefficients

The dose-response functions in the literature exhibit two distinct forms. The first form comprises two parts: the first part focusses on the influence of sulphur dioxide deposition rate, and the second part represents the impact of chloride deposition rate, as depicted in Equation 5-2.

$$R_{corr} = \mathrm{a1} \times P_d^{\mathrm{a2}} \times \tau^{\mathrm{a3}} \times e^{\mathrm{a4} \times T + \mathrm{a5}} + \mathrm{a6} \times S_d^{\mathrm{a7}} \times \tau^{\mathrm{a8}} \times e^{\mathrm{a9} \times T} \qquad 5\text{-}2$$

The coefficients in Equation 5-2 are determined using the least-squares method.

The second form can be found in Equation 5-3.

$$R_{corr} = \mathrm{b1} \times \left(\frac{\tau}{\mathrm{b2}}\right)^{\mathrm{b3}} \times \left(1 + \frac{P_d}{\mathrm{b4}}\right)^{\mathrm{b5}} \times \left(1 + \frac{S_d}{\mathrm{b6}}\right)^{\mathrm{b7}} \times e^{\mathrm{b8} \times (T + \mathrm{b9})} \qquad 5\text{-}3$$

The time of wetness adjustment factor $\left(\frac{\tau}{\mathrm{b2}}\right)^{\mathrm{b3}}$ reflects that corrosion does not occur in the absence of water. The value of b2 is set to 3384, which is equal to the mean of time of wetness values.

The sulphur dioxide adjustment factor $\left(1+\frac{P_d}{\mathrm{b4}}\right)^{\mathrm{b5}}$ includes P_d which ranges from 0.1 mg/(m²·d) to 4 mg/(m²·d), where the value of b4 is determined to be 1.7, i.e., the mean of sulphur dioxide values. The sulphur dioxide adjustment factor does not impact the corrosion rate when the sulphur dioxide concentration is zero, but it increases the rate when greater than zero. The chloride adjustment factor $\left(1+\frac{S_d}{\mathrm{b6}}\right)^{\mathrm{b7}}$ has the same form as the sulphur dioxide adjustment factor, and accounts for the possibility of non-zero corrosion rates even when chloride is zero. The value for b6 is determined to be 9.4, which is the mean of chloride values.

In general, the rate of corrosion tends to increase with higher temperatures. However, at temperatures below 0°C, there is a possibility of the electrolyte film freezing, which can cause a notable reduction in corrosion [101]. Conversely, at high temperatures, the moisture present on the surface tends to evaporate, leading to a slower corrosion rate [101]. The temperature adjustment factor, therefore, exhibits a distinctive form that differs from other environmental adjustment factors, as shown in Equation 5-4:

$$e^{\mathrm{b8}\times(T+\mathrm{b9})} \qquad 5\text{-}4$$

Corrosion tends to decrease as the temperature increases when the value of b8 is negative. Conversely, corrosion tends to increase as the temperature increases. For the calibration, the value of b9 in Equation 5-4 is set equal to 18.7 which is the mean of temperature values. The values of b1, b3, b5, b7 and b8 are then determined using the least-squares method. In this study, the coefficient calculation using the least-squares method is conducted using Python, utilizing the gradient descent algorithm. Starting from an initial point, an iterative process is employed to minimize the sum of squared residuals between the measured values and the computed values. The obtained coefficients for the two calibrated dose-response functions are presented in Table 5-4.

Table 5-4. Values of all coefficients present in the calibrated dose-response functions.

Eq.	a1	a2	a3	a4	a5	a6	a7	a8	a9
5-2	7.93	-0.15	0.1	-0.04	0	2.3e-4	-0.12	0.73	0.19
Eq.	b1	b2	b3	b4	b5	b6	b7	b8	b9
5-3	16.4	3384	0.3	1.7	0.01	9.4	0.3	0.002	18.7

5.2.4 Comparison of the models

After determining the optimized parameters, the above two dose-response functions are then used to calculate the corrosion rates based on the environmental variables from the corrosion dataset. A comparative analysis is then conducted against the measured corrosion rates. Figure 5-5 provides an initial assessment of the predictive performance of the two calibrated dose-response functions in relation to the measured values of corrosion rates. The graphical representation clearly demonstrates that function 5-3 exhibits a closer proximity between the predicted values and the measured values, indicating a superior fitting performance compared to function 5-2. This is also the case when we scrutinize the averages of predicted-to-measured ratios and the standard deviations, which equal 1.12 and 0.32 for function 5-3, while 1.23 and 0.80 for function 5-2. The red-shaded area shown in Figure 5-5 represents the 95% confidence interval associated with the predicted corrosion rates. In comparison to function 5-2, function 5-3 has a greater number of measured values of corrosion rates (18 data points) falling within this confidence interval. This suggests that function 5-3 efficiently predicts the corrosion rates, and in a way better than function 5-2 (10 data points).

In order to further identify an optimal dose-response function, four evaluation metrics are employed, which are R-squared (R^2), mean square error (MSE), root mean square error (RMSE), and mean absolute error (MAE) (see Equation 5-5 to 5-8). It should be noted that the higher values of R^2 and the lower values of MSE, RMSE and MAE indicate a good performance of the predictive function. The

evaluation metrics of two calibrated functions are shown in Table 5-5. It is clear that Equation 5-3 exhibits the smallest values of MSE (9.29), RMSE (3.05), and MAE (2.44) as well as the largest value of R^2 (0.66). In other words, Equation 5-3 outperforms Equation 5-2 in predicting the corrosion rate of carbon steel. As a result, Equation 5-3 has been demonstrated as the optimal choice for predicting the first-year corrosion rate of carbon steel in the natural environments with similar climatic conditions to this study.

$$R^2 = 1 - \frac{\sum(f_i - y_i)^2}{\sum(y_i - \bar{y})^2} \quad 5\text{-}5$$

$$MSE = \frac{1}{n}\sum_{i=1}^{n}(f_i - y_i)^2 \quad 5\text{-}6$$

$$RMSE = \sqrt{\frac{1}{n}\sum_{i=1}^{n}(f_i - y_i)^2} \quad 5\text{-}7$$

$$MAE = \frac{1}{n}\sum_{i=1}^{n}|f_i - y_i| \quad 5\text{-}8$$

where n is the number of data points, f_i is the predicted value, y_i is the corresponding real-measured value, and $\bar{y}$ is the mean value derived from the real-measured data.

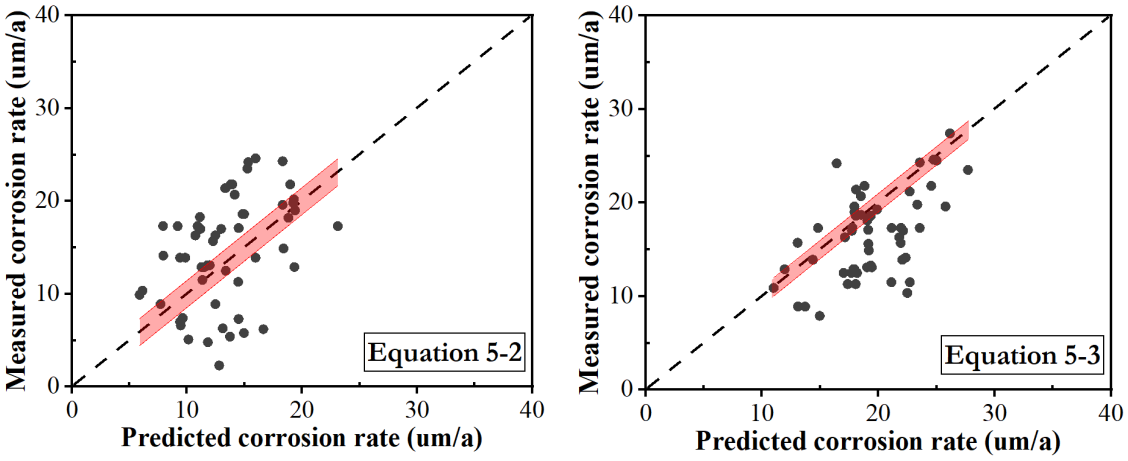

Figure 5-5. Predicted corrosion rates versus two different calibrated dose-response functions.

Table 5-5. Evaluation metrics for the two calibrated dose-response functions.

Function	R^2	MSE	RMSE	MAE
5-2	0.22	37.9	6.16	4.98
5-3	0.66	9.29	3.05	2.44

5.3 Overfitting test

To check that the models are not overfitting, the corrosion data samples are generally divided into a training set, which constitutes 80% of the dataset, and a testing set, representing the remaining 20% of the dataset. The training set is utilized to calibrate the coefficients of the environmental variables, while the testing set is used to evaluate the predictive performance of the calibrated function. These two datasets play a pivotal role in assessing whether the function exhibits overfitting behaviour. Overfitting refers to an undesirable statistical behaviour in which a function performs well in predicting training data but fails to generalize effectively to testing data. When a function overfits, it lacks the ability to accurately predict the outcomes in unseen data scenarios, thereby defeating its purpose. In this study, we can conclude that there is no evident overfitting, as there is no significant disparity in prediction accuracy between the training and testing sets (Table 5-6). Consequently, we can assume that the dose-response function 5-3 effectively captures the relationship between the input environmental variables and the corrosion rate.

Table 5-6. Evaluation metrics of the training dataset and testing dataset for the calibrated dose-response function 5-3.

Dataset	R^2	MSE	RMSE	MAE
Training data	0.66	9.29	3.05	2.44
Testing data	0.52	22.05	4.70	4.02

5.4 Variables significance

The coefficient-calibrated function, represented by Equation 5-9, distinctly reveals that the influence of sulphur dioxide on the corrosion rate is relatively insignificant compared to other variables. When the sulphur dioxide value changes from 0 mg/(m²·d) to 4 mg/(m²·d), the sulphur dioxide adjustment factor only varies by 0.012, which can be considered negligible. Consequently, it is reasonable to simplify the functional form by omitting the sulphur dioxide adjustment factor $\left(1+\frac{P_d}{1.7}\right)^{0.01}$ when the sulphur dioxide is within P0 level.

$$R_{corr} = 16.4 \times \left(\frac{\tau}{3384}\right)^{0.3} \times \left(1+\frac{P_d}{1.7}\right)^{0.01} \times \left(1+\frac{S_d}{9.4}\right)^{0.3} \times e^{0.002\times(T+18.7)} \qquad 5\text{-}9$$

The permutation importance method provides a more robust assessment of variable importance in the model by systematically permuting its values while keeping the remaining variables unchanged. By evaluating the resulting impact on the model's prediction accuracy, the significance of the variable can be determined. If a variable has a substantial influence on the model's predictions, permuting its values will lead to a noticeable decrease in prediction accuracy. Conversely, if permuting the values has minimal effect on the predictions, it suggests that the variable holds little importance for the model. As shown in Figure 5-6, where the variables are arranged on the vertical axis, the importance indicate that the temperature is identified as the most influential factor, followed by time of wetness. Chloride and sulphur dioxide, on the other hand, exhibit relatively lower levels of importance. Specifically, when sulphur dioxide deposition rate is at the P0 level, its impact on the corrosion rate is significantly lower compared to that of chloride.

In this study, Knokke-Heist, located near the North Sea and affected by Atlantic monsoons, experienced the highest corrosion rates due to the impact of chloride

ions [116]. Casalinho da Foz also experienced severe atmospheric corrosion and its high corrosion rates can be related to the high levels of both humidity and temperature, which can directly impact corrosion rate by affecting the stability of the electrolyte layer on the steel surface [117]. Air humidity creates a thermodynamically desirable state for electrochemical reactions to happen on the steel surface [116]. Higher temperature tends to accelerate both electrochemical reactions and diffusion processes but can result in greater evaporation of the electrolyte layer [98, 117]. In conclusion, high humidity combined with appropriately high temperature in Casalinho da Foz provide very favourable condition for corrosion process to happen. Moreover, even though the sulphur dioxide deposition rate in Oxford was 2 times higher than in Sint-Katelijne-Waver, there was minimal difference in the corrosion rates. It should be noted that despite the little difference in the environmental factor levels of humidity, temperature, and sulphur dioxide deposition rate, there was significant difference in the corrosion rates observed in Sint-Katelijne-Waver and Knokke-Heist, suggesting that chloride deposition increases the sensitivity to uniform corrosion.

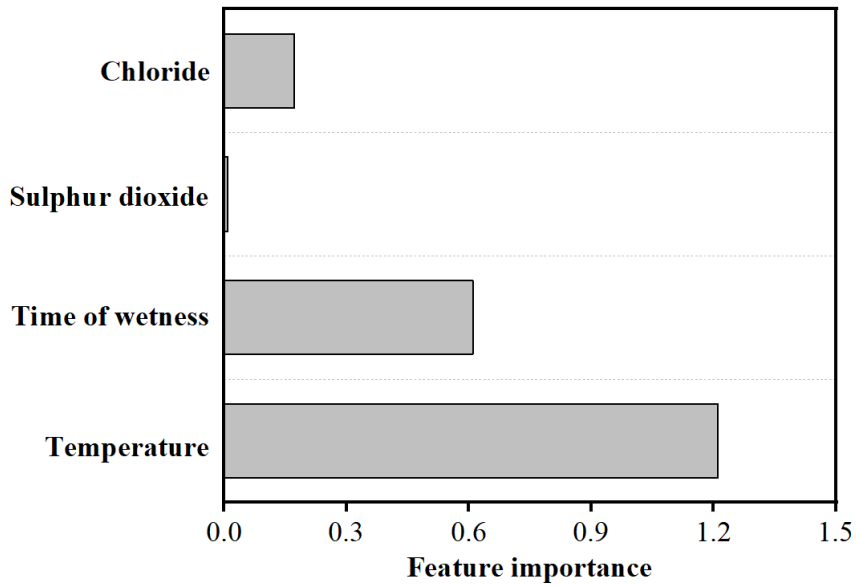

Figure 5-6. Importance of each variable in the dose-response function 5-3.

6

Conclusions

This work focusses on the corrosion on dissimilar welded T-joints between duplex stainless steel (EN1.4062) and carbon steel (both S355J2 and P460NL2) in mildly corrosive atmospheric environments. The conclusions presented in this section are based on a series of experiments (atmospheric corrosion tests) carried out in four different European locations (Sint-Katelijne-Waver, Oxford, Casalinho da Foz and Knokke-Heist) as well as a database of similar tests gathered from the literature.

The following conclusions were drawn:

1. Uniform corrosion occurred on all carbon steel samples as expected. Our corrosion rate measurements indicate that both carbon steel grades exhibited significantly higher corrosion rates compared to the duplex stainless steel which can be attributed to the absence of a self-repairing protective layer on the carbon steel. This was an expected behaviour. Rust formation was initially observed in the heat-affected zone of carbon steel, subsequently spreading to the base metal. No corrosion was observed on the surface of the duplex stainless steel, nor across the weld metal or at the edges of the T-joint samples. This can be explained by the presence of a protective layer consisting of chromium-rich oxides and hydroxides, forming a self-repairing passive film on the metal surface which is an inherent characteristic of stainless steel. The

corrosion rates of carbon-removed dissimilar welds, EN1.4062/309LSi, did not exceed 2.5 μm/a. This suggests that the occurrence of uniform corrosion at the stainless steel junctions was not influenced by welding. This can be attributed to the choice of the right combination of welding process parameters (voltage, current, heat input and arc travel speed) and appropriate selection of filler material.

2. Localized and galvanic corrosions occurred. The heat-affected zone of carbon steel exhibited more severe localized corrosion, which can be attributed to decarburization and grain growth resulting from element diffusion during the welding process. The pits found in the heat-affected zone of the carbon steel grades were notably deeper in Knokke-Heist due to high chloride deposition rate. Conversely, no pitting was detected in the heat-affected zone between the austenitic 309LSi filler and the EN1.4062 lean duplex stainless steel. Pitting resistance is once again due to the formation of the protective film on both grades, which offer superior corrosion resistance. A galvanic corrosion experiment conducted in seawater indicated that the average potential difference between duplex EN1.4062 and carbon steels (S355J2 and P460NL2) was +0.41 V. This experiment demonstrated the possibility of spontaneous galvanic corrosion of carbon steel if in the right corrosive environment.

3. Two key parameters, temperature and time of wetness, primarily influence atmospheric corrosion rates, while the chloride deposition rate has a greater influence on localized corrosion rather than on the overall atmospheric corrosion rates. Knokke-Heist is the test site that exhibited the highest level of corrosivity to the carbon steel base plates and the dissimilar welded joints. This was expected because of its geographical location characterised by the

highest chloride deposition rate. Casalinho da Foz, despite having lower sulphur dioxide and chloride deposition rates, exhibited higher corrosivity due to its highest temperature and time of wetness. The elevated temperature and time of wetness create a more corrosive environment by facilitating increased moisture retention on the surface of the materials. The prolonged presence of moisture enhances the corrosion process, even in the absence of higher levels of chloride or sulphur dioxide. Oxford and Sint-Katelijne-Waver, being at greater distances from the coastline, exhibit lower corrosion rates. The long distance from the coastline helps reduce the exposure to chloride-rich atmosphere, and the milder environmental conditions, i.e., lower temperature and time of wetness, further mitigate the corrosive effects. This combination of factors results in lower overall corrosion behaviours compared to Knokke-Heist and Casalinho da Foz.

4. The discontinuous interface between the weld nugget and the carbon steel plates is shown to be sensitive to pitting corrosion, especially when the dissimilar weld is subjected to a chloride-rich environment (here Knokke-Heist). At the galvanic zones (between the carbon steel and stainless steel plates), the susceptibility to galvanic corrosion is higher. In NORSOK M-501 [118], it is recommended to coat the stainless steel plates when welded to carbon steel across a depth of 50 mm. Based on the experiments conducted in this research, we confirm that recommendation if the environment has a CRF value of -7 or lower, especially if the heat-affected zones and galvanic zones are exposed to salt-rich atmospheric environments (i.e., close distance to the sea or presence of de-icing salt). However, we noticed that dissimilar welds in location sites with a CRF value of -3 or higher are not susceptible to pitting corrosion (within 12 months exposure) hence coating stainless steel in this instance appears to be a conservative measure.

5. The prediction of the obtained and gathered corrosion rates based on the weather parameters revealed that the empirical formula provided in ISO 9223 is not sufficiently conservative, whereas the empirical formula proposed by Klinesmith et al. leads to too conservative results. Factors such as dissimilar welding, galvanic corrosion, and localized corrosion are not considered in the formula which can explain the reason for the conservatism especially for chloride-rich environments. Therefore, the coefficients of the dose-response function were reassessed. To do this, Spearman correlation analysis was employed to screen and identify the key environmental variables. Literature results where similar grades were studied and for test sites with similar climatic conditions (i.e., deposition rate of sulphur dioxide at P0 level, deposition rate of chloride at S1 level, the duration of wetness at τ4 level) were gathered. The coefficients of the environmental variables were calibrated in two selected dose-response functions, and a more accurate function predicting the corrosion rates was derived by considering a range of evaluation metrics (R^2, MSE, RMSE, MAE). The permutation importance method further validated the significance of four key weather parameters: temperature, time of wetness, sulphur dioxide deposition rate, and chloride deposition rate. These parameters were identified as crucial factors in determining the corrosion rate of carbon steels.

REFERENCES

[1] EN ISO 8501-1: Preparation of steel substrates before application of paints and related products - visual assessment of surface cleanliness - part 1: Rust grades and preparation grades of uncoated steel substrates and of steel substrates after overall removal of previous coatings. Brussels, Belgium: European Committee for Standardization, 2007.

[2] Y. Cools and A. Staepels. "Microstructural and mechanical investigations on dissimilar welding". *Master of Science*. Leuven, Belgium: Ku Leuven, 2021.

[3] Y. Bouassida et al. "Bridge design to eurocodes worked examples". *Bridge Design to Eurocodes*. Vienna, 2010.

[4] K. Sterckx and N. V. Broecke. "Painted, stainless or hybrid steel box girder bridges: Comparative life cycle cost assessment". *Master of Science*. Leuven, Belgium: Ku Leuven, 2020.

[5] B. Karabulut et al. "Lifecycle cost assessment of high strength carbon and stainless steel girder bridges". *J Environ Manage*. **277** (2021): 1-15.

[6] T. Yabuki et al. "Hybrid stainless steel girder for bridge construction". *International Scholarly and Scientific Research & Innovation*. **11** (5) (2017): 648-655.

[7] C. Li et al. "Microstructures and mechanical properties of stainless steel clad plate joint with diverse filler metals". *Journal of Materials Research and Technology*. **9** (2) (2020): 2522-2534.

[8] R. Sathish et al. "Weldability and process parameter optimization of dissimilar pipe joints using gtaw". *International Journal of Engineering Research and Applications*. **2** (3) (2012): 2525-2530.

[9] P. Sędek et al. "Residual stress relief in mag welded joints of dissimilar steels". *International Journal of Pressure Vessels and Piping*. **80** (10) (2003): 705-713.

[10] E. Ranjbarnodeh et al. "Effect of welding parameters on residual stresses in dissimilar joint of stainless steel to carbon steel". *Journal of Materials Science*. **46** (9) (2010): 3225-3232.

[11] I. O. Oladele et al. "Comparative investigation of the mechanical properties and corrosion behaviour of dissimilar metal weld fusion zone, heat affected zones and base metal". *International Journal of Engineering*. **16** (1) (2018): 187-192.

[12] G. Pimenta and R. A. Jarman. "Corrosion of metal joints". *Materials Science and Materials Engineering*. **3** (2010): 2447-2462.

[13] I. Hajiannia et al. "Microstructure and mechanical properties of aisi 347 stainless steel/a335 low alloy steel dissimilar joint produced by gas tungsten arc welding". *Materials and Design*. **50** (2013): 566-573.

[14] J. K. Kim et al. "Microstructure and high temperature properties of the dissimilar weld between ferritic stainless steel and carbon steel". *Metals and Materials International*. **15** (5) (2009): 843-849.

[15] K. Kimapong and S. Triwanapong. "Microstructure and bending strength of dissimilar ss400/sus304 steels t-fillet joint by gas metal arc welding". *Key Engineering Materials*. **773** (2018): 189-195.

[16] L. Liying et al. "Microstructure and mechanical properties of welded joints of l415/316l bimetal composite pipe using post internal-welding process". *International Journal of Pressure Vessels and Piping*. **179** (2020).

[17] D. K. Singh et al. "Investigation on the microstructure - mechanical property correlation in dissimilar steel welds of stainless steel ss 304 and medium carbon steel en 8". *Journal of Manufacturing Processes*. **36** (2018): 281-292.

[18] P. Luchtenberg et al. "Effect of welding energy on the corrosion and tribological properties of duplex stainless steel weld overlay deposited by gmaw/cmt process". *Surface and Coatings Technology*. **375** (2019): 688-693.

[19] W. Chuaiphan et al. "Dissimilar welding between aisi 304 stainless steel and aisi 1020 carbon steel plates". *Applied Mechanics and Materials*. **268-270** (2012): 283-290.

[20] S. Wang et al. "Characterization of microstructure, mechanical properties and corrosion resistance of dissimilar welded joint between 2205 duplex stainless steel and 16mnr". *Materials and Design*. **32** (2) (2011): 831-837.

[21] J. Wang et al. "Effect of welding process on the microstructure and properties of dissimilar weld joints between low alloy steel and duplex stainless steel". *International Journal of Minerals, Metallurgy, and Materials*. **19** (6) (2012): 518-524.

[22] H. Tasalloti et al. "Effect of heat input on dissimilar welds of ultra high strength steel and duplex stainless steel: Microstructural and compositional analysis". *Materials Characterization*. **123** (2017): 29-41.

[23] P. B. Srinivasan et al. "An assessment of impact strength and corrosion behaviour of shielded metal arc welded dissimilar weldments between uns 31803 and is 2062 steels". *Materials and Design*. **27** (3) (2006): 182-191.

[24] B. L. Bramfitt and A. O. Benscoter. *Metallographer's guide: Practices and procedures for irons and steels*. United States: ASM International, 2002.

[25] EN 10025-2: Hot rolled products of structural steels - technical delivery conditions for non-alloy structural steels. The British Standards Institution, 2019.

[26] EN 10025-3: Hot rolled products of structural steels - technical delivery conditions for normalized/normalized rolled weldable fine grain structural steels. The British Standards Institution, 2019.

[27] B. Karabulut and B. Rossi. "Fatigue behaviour of duplex welded details". *Doctor of Engineering Technology*. Leuven, Belgium: Ku Leuven, 2021.

[28] Individual and corporate membership. *Design manual for structural stainless steel*. Berkshire, the United Kingdom: The Steel Construction Institute, 2017.

[29] B. Karabulut et al. "Experimental and numerical fatigue assessment of duplex welded transversal stiffeners". *International Journal of Fatigue*. **134** (2020).

[30] N. R. Baddoo. "Stainless steel in construction: A review of research, applications, challenges and opportunities". *Journal of Constructional Steel Research*. **64** (11) (2008): 1199-1206.

[31] N. R. Baddoo and A. Kosmač. "Sustainable duplex stainless steel bridges". (2010).

[32] I. S. S. Forum. *Duplex stainless steel brochure*. Brussels, 2021.

[33] ISO 12944-2: Paints and varnishes - corrosion protection of steel structures by protective paint systems - part 2: Classification of environments. International Organization for Standardization, 2017.

[34] R. Merello et al. "Influence of chemical composition on the pitting corrosion resistance of non-standard low-ni high-mn–n duplex stainless steels". *Corros Sci*. **45** (2003): 909–921.

[35] J. Olsson and M. Snis. "Duplex - a new generation of stainless steels for desalination plants". *Desalination*. **205** (1-3) (2007): 104-113.

[36] Z. Wei et al. "Study of mechanical and corrosion properties of a fe–21.4cr–6mn–1.5ni–0.24n–0.6mo duplex stainless steel". *Materials Science and Engineering*. **497** (1-2) (2008): 501-504.

[37] A. K. Iversen. "Stainless steels in bipolar plates - surface resistive properties of corrosion resistant steel grades during current loads". *Corros Sci*. **48** (5) (2006): 1036-1058.

[38] V. V. Berezovskaya et al. "Corrosion properties of austenitic cr-mn-ni-n steels with various manganese concentrations". *Russian Metallurgy (Metally)*. **2008** (1) (2008): 29-33.

[39] J. Hicks. *Welded design - theory and practice*. Cambridge, England: Abington

Publishing, 2001.

[40] S. A. David et al. *Encyclopedia of materials: Science and technology*. Tennessee, United States: Pergamon, 2003.

[41] M. Onvani. "Dissimilar welding of s235jr to en1.4307 with 316lsi filler material". *Master of Science*. Leuven, Belgium: Ku Leuven, 2019.

[42] M. Khedr et al. "Review on the solid-state welding of steels: Diffusion bonding and friction stir welding processes". *Metals*. **13** (1) (2022).

[43] U. S. Dixit et al. *Mechanics of materials in modern manufacturing methods and processing techniques*. Amsterdam, Netherlands: Elsevier, 2020.

[44] S. Hashmi. *Welding processes and technologies*. Elsevier, 2014.

[45] F. Armao et al. *Gas metal arc welding guidelines*. Lincoln Electric Company, 2014.

[46] H. Pouraliakbar et al. "Designing of ck45 carbon steel and aisi 304 stainless steel dissimilar welds". *Materials Research*. **17** (1) (2013): 106-114.

[47] T. Maruyama. "Arc welding technology for dissimilar joints". *Journal of the Japan Welding Society*. **71** (2002): 25-29.

[48] P. Guiraldenq and O. Hardouin Duparc. "The genesis of the schaeffler diagram in the history of stainless steel". *Metallurgical Research & Technology*. **114** (6) (2017).

[49] L. Pilcher. "Australian stainless steel development association". *Aust Stainl Mag*. **316** (23) (2002): 2-4.

[50] J. R. Davis. *Metals handbook*. Metals Park, 1993.

[51] M. Iordachescu et al. "Thermal influence of welding process on strength overmatching of thin dissimilar sheets joints". *Proceedings of CIFIE 2010, Iberian Conference on Fracture and Structural integrity*. Oporto, Portugal, 2010.

[52] S. K. Mahmoud et al. "Study on microstructure and mechanical characteristics of low-carbon steel and ferritic stainless steel joints". *Materials Science and Engineering*. **608** (2014): 35-45.

[53] A. Moteshakker and I. Danaee. "Microstructure and corrosion resistance of dissimilar weld-joints between duplex stainless steel 2205 and austenitic stainless steel 316l". *Journal of Materials Science & Technology*. **32** (3) (2016): 282-290.

[54] E. J. Barnhouse and J. C. Lippold. "Microstructure/property relationships in dissimilar welds between duplex stainless steels and carbon steels". *Welding Journal*. **77** (12) (1998): 477-487.

[55] I. Mészáros. "Magnetic characterisation of duplex stainless steel". *Physica B: Condensed Matter*. **372** (1-2) (2006): 181-184.

[56] J. W. Fu et al. "Microstructure evolution in aisi 304 stainless steel during near rapid directional solidification". *Materials Science and Technology*. **25** (8) (2013): 1013-1016.

[57] A. F. Padilha et al. "Delta ferrite formation in austenitic stainless steel castings". *Materials Science Forum*. **730-732** (2012): 733-738.

[58] A. S. Hamada et al. "Fatigue behavior of ultrafine-grained and coarse-grained cr–ni austenitic stainless steels". *Materials Science and Engineering: A*. **528** (10-11) (2011): 3890-3896.

[59] N. Alcantar-Modragón et al. "Study of cracking susceptibility in similar and dissimilar welds between carbon steel and austenitic stainless steel through finger test and fe numerical model". *The International Journal of Advanced Manufacturing Technology*. (2021).

[60] H. Ma et al. "Microstructure characterization and properties of carbon steel to stainless steel dissimilar metal joint made by friction welding". *Mater Design*. **86** (2015): 587-597.

[61] A. Hamid et al. "Failure of weld joints between carbon steel pipe and 304 stainless steel elbows". *Eng Fail Anal*. **12** (2) (2005): 181-191.

[62] S. H. Lee. "A hot cracking on dissimilar metal weld between a106gr.B and a312 tp316l with buttering ernicr-3". *Metals*. **9** (5) (2019).

[63] F. Kauffmann et al. "Creep behavior and in-depth microstructural characterization of dissimilar joints". *Sci Technol Adv Mater*. **14** (1) (2013): 014203.

[64] H. Tasalloti et al. "Effects of welding wire and torch weaving on gmaw of s355mc and aisi 304l dissimilar welds". *The International Journal of Advanced Manufacturing Technology*. **71** (1-4) (2013): 197-205.

[65] H. Li et al. "Investigating the inter-relationships among multiple atmospheric variables and their responses to precipitation". *Atmosphere*. **14** (3) (2023).

[66] Y. Zhi et al. "Improving atmospheric corrosion prediction through key environmental factor identification by random forest-based model". *Corros Sci*. **178** (2021).

[67] W. Han et al. "A study on the initial corrosion behavior of carbon steel exposed to outdoor wet-dry cyclic condition". *Corros Sci*. **88** (2014): 89-100.

[68] W. Han et al. "Characterisation of initial atmospheric corrosion carbon steels by

field exposure and laboratory simulation". *Corros Sci*. **49** (7) (2007): 2920-2935.

[69] I. M. Allam et al. "Initia stages of atmospheric corrosion of steel in the arabian gulf". *Corros Sci*. **32** (4) (1991): 417-432.

[70] J. Weissenrieder and C. Leygraf. "In situ studies of filiform corrosion of iron". *J Electrochem Soc*. **151** (3) (2004).

[71] R. S. T. J. Preston and B. Sanyal. "Atmospheric corrosion by nuclei". *Journal of Applied Chemistry*. **6** (1) (1956): 26-44.

[72] Outokumpu. *Handbook of stainless steel*. Finland: Outokumpu Oyj, 2013.

[73] P. R. Roberge. *Corrosion engineering: Principles and practice*. United States of America: The McGraw-Hill Companies, 2008.

[74] Specialty Steel Industry of North American: "Galvanic corrosion". *https://www.ssina.com/education/corrosion/galvanic-corrosion/* (*Access date*: Sep 2022).

[75] D. Fuente et al. "Characterisation of rust surfaces formed on mild steel exposed to marine atmospheres using xrd and sem/micro-raman techniques". *Corros Sci*. **110** (2016): 253-264.

[76] S. Fonna et al. "Investigation of corrosion products formed on the surface of carbon steel exposed in banda aceh's atmosphere". *Heliyon*. **7** (4) (2021): 1-13.

[77] T. Ogawa and T. Koseki. "Effect of composition profiles on metallurgy and corrosion behavior of duplex stainless steel weld metals". *Welding Journal*. **68** (5) (1989).

[78] S. Hertzman and E. Symniotis. "Stainless steel '91". *Int Conf on Stainless Steels*. Chiba Japan: The Iron and Steel Institute of Japan, 1997.

[79] C. C. Hsieh and W. Wu. "Overview of intermetallic sigma (σ) phase precipitation in stainless steels". *ISRN Metallurgy*. **2012** (2012): 1-16.

[80] H. Song et al. "Heat-treatment of clad steel plate for application of hull structure". *Ocean Eng*. **122** (2016): 278-287.

[81] E. M. Westin. "Microstructure and properties of welds in the lean duplex stainless steel ldx 2101". *Doctor of Engineering Technology*. Sweden: Royal Institute of Technology, 2010.

[82] R. A. Walker. "Duplex and high alloy stainless steels – corrosion resistance and weldability". *Materials Science and Technology*. **4** (1) (2013): 78-84.

[83] T. E. Abioye et al. "Effects of welding speed on the microstructure and corrosion behavior of dissimilar gas metal arc weld joints of aisi 304 stainless steel and low

carbon steel". *Materials Today: Proceedings*. **17** (2019): 871-877.

[84] EN 1993-1-4: Eurocode 3 - design of steel structures. The British Standards Institution, 2006.

[85] EN ISO 8565: Metals and alloys - atmospheric corrosion testing - general requirements. Brussels, Belgium: European Committee for Standardization, 2011.

[86] Corus. *Corrosion protection of steel bridges*. North Lincolnshire, the United Kingdom: Orchard Corporate Ltd., 2005.

[87] EN ISO 9225: Corrosion of metals and alloys - corrosivity of atmospheres - measurement of environmental parameters affecting corrosivity of atmospheres. Brussels, Belgium: European Committee for Standardization, 2012.

[88] ASTM G1-90: Standard practice for preparing, cleaning, and evaluating corrosion test specimens. Pennsylvania, United States: American Society for Testing and Materials, 1999.

[89] EN ISO 9223: Corrosion of metals and alloys - corrosivity of atmospheres - classification, determination and estimation. Brussels, Belgium: European Committee for Standardization, 2012.

[90] E. Schindelholz and R. G. Kelly. "Wetting phenomena and time of wetness in atmospheric corrosion: A review". *Corros Rev*. **30** (5-6) (2012).

[91] European Environment Agency: "Air quality statistics". *http://aidef.apps.eea.europa.eu/* (*Access date*: Sep 2022).

[92] R. E. Melchers. "Effect of small compositional changes on marine immersion corrosion of low alloy steels". *Corros Sci*. **46** (7) (2004): 1669-1691.

[93] M. Reffass et al. "Localised corrosion of carbon steel in nahco3/nacl electrolytes: Role of fe(ii)-containing compounds". *Corros Sci*. **48** (3) (2006): 709-726.

[94] J. Guo et al. "Electrochemical behavior and surface composition of copper containing ferritic stainless steel in sulfuric acid solution". *Boshoku Gijutsu*. **32** (1986): 283-288.

[95] A. Higginson et al. "The passivation of fe-cr-ru alloys in acidic solutions". *Corros Sci*. **29** (11) (1989): 1293-1318.

[96] G. Su and X. Gao. "Comparison of medium manganese steel and q345 steel on corrosion behavior in a 3.5 wt % nacl solution". *Materials (Basel)*. **10** (8) (2017).

[97] X. Gao et al. "Evolution of the rust layers formed on carbon and weathering steels in environment containing chloride ions". *Acta Metallurgica Sinica (English Letters)*. **29** (11) (2016): 1025-1036.

[98] A. M. A. Mohamed and P. Okonkwo. "Environmental factors affecting corrosion of pipeline steel: A review". *International Journal of Mechanical and Production Engineering Research and Development*. **5** (5) (2015): 57-70.

[99] L. T. H. Lien and P. T. San. "The effect of environmental factors on carbon steel atmospheric corrosion: The prediction of corrosion". *Outdoor atmospheric corrosion*. West Conshohocken, Pennsylvania: ASTM special technical publication, 2002.

[100] D. Knotkova et al. "Results from the multi-pollutant programme corrosion attack on carbon steel after 1, 2 and 4 years of exposure (1997–2001)". *UN/ECE International Co-operative Programme on Effect on Materials, including Historic and Cultural Monuments*. Prague, Czech Republic: Institute for Protection of Material, 2003.

[101] D. E. Klinesmith et al. "Effect of environmental conditions on corrosion rates". *J Mater Civ Eng*. **19** (2) (2007): 121-129.

[102] D. Knotkova et al. *International atmospheric exposure program: Summary of results*. Pennsylvania, United States, 2010.

[103] M. M. Mukaka. "Statistics corner: A guide to appropriate use of correlation coefficient in medical research". *Malawi Medical Journal*. **24** (3) (2012): 69-71.

[104] J. Tidblad et al. "Model for the prediction of the time of wetness from average annual data on relative air humidity and air temperature". *Prot Met+*. **36** (6) (2000): 533–540.

[105] M. Hoseinpoor et al. "Toward more realistic time of wetness measurement by means of surface relative humidity". *Corros Sci*. **177** (2020).

[106] B. Chico et al. "Annual atmospheric corrosion of carbon steel worldwide. An integration of isocorrag, icp/unece and micat databases". *Materials (Basel)*. **10** (6) (2017).

[107] D. D. N. Singh et al. "Role of climatic conditions on corrosion characteristics of structural steels". *Corros Sci*. **50** (1) (2008): 93-110.

[108] J. F. Marco et al. "Characterization of the corrosion products formed on carbon steel after exposure to the open atmosphere in the antarctic and easter island". *Corros Sci*. **42** (2000): 753-771.

[109] J. Huang et al. "Atmospheric corrosion of carbon steels in tropical and subtropical climates in southern china". *Materials and Corrosion*. **71** (8) (2020): 1400-1406.

[110] C. Sica et al. "Atmospheric corrosion performance of carbon steel, galvanized steel, aluminum and copper in the north brazilian coast". *J Braz Chem Soc*. **18** (1) (2007): 153-166.

[111] W. Thandar et al. "Investigation of initial atmospheric corrosion of carbon and weathering steels exposed to urban atmospheres in myanmar". *International Journal of Corrosion*. **2022** (2022): 1-10.

[112] Y. Seechurn et al. "Marine atmospheric corrosion of carbon steel in the tropical microclimate of port louis". *Materials and Corrosion*. **73** (9) (2022): 1474-1489.

[113] T. Prosek and J. Tidblad. *Catalogue of atmospheric corrosion field exposure sites in europe*. 2021.

[114] S. K. Coburn et al. "Corrosivennes of various atmospheric test sites as measured by specimens of steel and zinc". *Metal Corrosion in the Atmosphere*. Philadelphia, USA: American Society for Testing and Materials, 1968.

[115] N. S. Palsson et al. "Outdoor atmospheric corrosion of carbon steel and weathering steel exposed to the tropical - coastal climate of thailand". *Materials and Corrosion*. **71** (6) (2019): 1019-1034.

[116] M. Shiri and D. Rezakhani. "Estimated and stationary atmospheric corrosion rate of carbon steel, galvanized steel, copper and aluminum in iran". *Metallurgical and Materials Transactions*. **51** (1) (2019): 342-367.

[117] R. Vera et al. "Atmospheric corrosion of copper exposed to different environments in the region of valparaiso, chile". *Materials and Corrosion*. **68** (3) (2017): 316-328.

[118] NORSOK M-501: Surface preparation and protective coating. Norway: Standards Norway, 2004.

APPENDIX A

One can see the values of $F1$, $F2$ and $F3$ which consider the risk of exposure to chlorides from salt water or de-icing salts, risk of exposure to sulphur dioxide and the cleaning regime or exposure to washing by rain in Table A.

Table A. Determination of Corrosion Resistance Factor (CRF) [84].

$F1$ Risk of exposure to chlorides from salt water or de-icing salts		
NOTE: M is distance from the sea and S is distance from roads with de-icing salts.		
1	Internally controlled environment	
0	Low risk of exposure	$M > 10$ km or $S > 0.1$ km
-3	Medium risk of exposure	1 km < $M \leq 10$ km or 0.01 km < $S \leq 0.1$ km
-7	High risk of exposure	0.25 km < $M \leq 1$ km or $S \leq 0.01$ km
-10	Very high risk of exposure	Road tunnels where de-icing salt is used or where vehicles might carry de-icing salts into the tunnel
-10	Very high risk of exposure	$M \leq 0.25$ km North Sea coast of Germany and all Baltic coastal areas
-15	Very high risk of exposure	$M \leq 0.25$ km Atlantic coastline of Portugal, Spain and France. English Channel and North Sea Coastline of UK, France, Belgium, Netherlands and Southern Sweden. All other coastal areas of UK, Norway, Denmark and Ireland. Mediterranean Coast
$F2$ Risk of exposure to sulphur dioxide		
For European coastal environments the sulphur dioxide concentration is usually low. For inland environments the sulphur dioxide concentration is either low or medium. The high classification is unusual and associated with particularly heavy industrial locations or specific environments such as road tunnels. Sulphur dioxide concentration may be evaluated according to the method in [87].		
0	Low risk of exposure	< 10 μg/m^3 average gas concentration
-5	Medium risk of exposure	10 - 90 μg/m^3 average gas concentration
-10	High risk of exposure	90 - 250 μg/m^3 average gas concentration
$F3$ Cleaning regime or exposure to washing by rain (if $F1+F2 \geq 0$, then $F3 = 0$)		
0	Fully exposed to washing by rain	
-2	Specified cleaning regime	
-7	No washing by rain or no specified cleaning	
If the component is to be regularly inspected for any signs of corrosion and cleaned, this should be made clear to the user in written form. The inspection, cleaning method and frequency should be specified. The more frequently cleaning is carried out, the greater the benefit. The frequency should not be less than every 3 months. Where cleaning is specified, it should apply to all parts of the structure, and not just those easily accessible and visible.		

APPENDIX B

Table B. Database of corrosion tests used in this study compiled from literature sources.

Code	Location	Grade	T [°C]	τ [h/a]		P_d [mg/(m²·d)]		S_d [mg/(m²·d)]		R_{corr} [µm/a]		Ref.
1	Iguazu	AISI 1006	22.9	5387	τ4	2.0	P0	1.5	S0	5.8	C2	[102]
2	San Juan	AISI 1006	19.2	911	τ3	2.0	P0	1.5	S0	4.6	C2	[102]
3	Ahtari	AISI 1006	4.0	3040	τ4	2.8	P0	1.5	S0	9.7	C2	[102]
4	Ahtari	AISI 1006	4.0	3127	τ4	2.5	P0	1.5	S0	12.5	C2	[102]
5	Ahtari	AISI 1006	4.1	3381	τ4	1.5	P0	1.5	S0	11.3	C2	[102]
6	Birkenes	AISI 1006	5.2	3679	τ4	1.4	P0	0.6	S0	21.4	C2	[102]
7	Birkenes	AISI 1006	5.9	4608	τ4	1.0	P0	0.6	S0	18.6	C2	[102]
8	Birkenes	AISI 1006	6.3	4187	τ4	1.0	P0	0.6	S0	21.8	C2	[102]
9	Birkenes	AISI 1006	7.5	4406	τ4	0.8	P0	0.6	S0	17.1	C2	[102]
10	Birkenes	AISI 1006	6.6	3968	τ4	0.8	P0	0.6	S0	20.7	C2	[102]
11	Birkenes	AISI 1006	6.2	3679	τ4	0.8	P0	0.6	S0	18.6	C2	[102]
12	EI Pardo	AISI 1006	25.3	2427	τ3	3.1	P0	1.5	S0	16.3	C2	[106]
13	EI Pardo	AISI 1006	25.3	2716	τ4	3.8	P0	1.5	S0	17.0	C2	[106]
14	EI Pardo	AISI 1006	25.2	3522	τ4	3.3	P0	1.5	S0	15.6	C2	[106]
15	Los Angeles	CS	17.4	1956	τ3	0.5	P0	33.0	S1	17.3	C2	[106]

16	San Juan	CS	18.8	902	τ3	2.0	P0	1.5	S0	4.9	C2	[106]
17	Caratinga	CS	21.5	4222	τ4	0.8	P0	8.9	S1	8.6	C2	[106]
18	Caratinga	CS	20.9	4222	τ4	1.3	P0	7.4	S1	11.5	C2	[106]
19	Caratinga	CS	21.2	4222	τ4	1.7	P0	1.6	S0	13.1	C2	[106]
20	Brasilia	CS	20.4	3872	τ4	2.0	P0	1.5	S0	12.9	C2	[106]
21	Paulo Afonso	CS	25.9	1507	τ3	2.0	P0	1.5	S0	17.3	C2	[106]
22	Cotove	CS	27.0	2891	τ4	0.3	P0	1.5	S0	19.6	C2	[106]
23	/	CS	14.4	3504	τ4	0.7	P0	20.0	S1	24.5	C2	[114]
24	/	CS	7.5	4406	τ4	0.3	P0	2.7	S0	6.2	C2	[114]
25	/	CS	6.6	3968	τ4	0.6	P0	29.1	S1	23.5	C2	[114]
26	/	CS	15.3	4845	τ4	0.3	P0	2.7	S0	5.4	C2	[114]
27	/	CS	14.2	1500	τ3	0.8	P0	3.0	S1	7.4	C2	[114]
28	Chennai	CS	28.3	2791	τ4	0.9	P0	1.7	S0	19.0	C2	[107]
29	Delhi	CS	25.5	702	τ3	0.2	P0	2.3	S0	13.9	C2	[107]
30	Digha	CS	26.6	2280	τ3	1.0	P0	0.8	S0	24.2	C2	[107]
31	Easter Island	SAE 1070	20.5	4690	τ4	1.2	P0	50.0	S1	30.0	C2	[108]
32	Mawlamyine	CS	23.8	5532	τ4	2.4	P0	1.9	S0	13.9	C2	[111]
33	Yangon	CS	28.9	4002	τ4	2.4	P0	3.7	S1	17.3	C2	[111]
34	Mandalay	CS	28.6	1172	τ3	2.4	P0	1.2	S0	8.9	C2	[111]
35	Rajiv Gandhi	S235	28.0	1798	τ3	1.4	P0	57.3	S1	3.7	C2	[112]

36	Fort George	S235	28.0	1800	τ3	1.9	P0	41.6	S1	5.7	C2	[112]
37	Mutual Aid	S235	28.3	1800	τ3	1.4	P0	14.5	S1	2.3	C2	[112]
38	Medine Camp de Masque	S235	26.3	3272	τ4	1.6	P0	51.4	S1	6.3	C2	[112]
39	Xishuangbanna	Q345	21.5	4320	τ4	0.1	P0	0.1	S0	14.9	C2	[109]
40	Kralupy	CS	11.0	3679	τ4	4.0	P0	1.0	S0	5.1	C2	[113]
41	Phangnga	CS	27.7	5090	τ4	2.6	P0	28.6	S1	18.2	C2	[115]
42	Prague	CS	11.0	3592	τ4	4.0	P0	3.0	S0	7.0	C2	[113]
43	Berlin	CS	10.0	4030	τ4	1.6	P0	12.0	S1	4.8	C2	[113]
44	Barcelona	CS	15.0	4468	τ4	3.0	P0	3.0	S0	6.6	C2	[113]
45	Birkenes	CS	6.0	3942	τ4	1.0	P0	7.0	S1	7.3	C2	[113]
46	UEMA	CS	27.2	4920	τ4	2.8	P0	8.3	S1	21.8	C2	[110]
47	Santa Rita	CS	27.8	3420	τ4	3.0	P0	16.6	S1	24.6	C2	[110]
48	Miranda	CS	28.2	3390	τ4	2.0	P0	13.0	S1	24.3	C2	[110]
49	São Mateus	CS	28.2	3897	τ4	1.9	P0	9.5	S1	19.8	C2	[110]
50	Peritoró	CS	28.5	3560	τ4	1.3	P0	9.5	S1	20.2	C2	[110]